12-2016

Analysis of composite plates by using mechanics of structure genome and comparison with ANSYS

Banghua Zhao
Purdue University

Graduate School Form
30 Updated 12/26/2015

PURDUE UNIVERSITY
GRADUATE SCHOOL
Thesis/Dissertation Acceptance

This is to certify that the thesis/dissertation prepared

By Banghua Zhao

Entitled

ANALYSIS OF COMPOSITE PLATES BY USING MECHANICS OF STRUCTURE GENOME AND COMPARISON WITH ANSYS

For the degree of Master of Science in Aeronautics and Astronautics

Is approved by the final examining committee:

Wenbin Yu
Chair

Tyler N. Tallman

Vikas Tomar

To the best of my knowledge and as understood by the student in the Thesis/Dissertation Agreement, Publication Delay, and Certification Disclaimer (Graduate School Form 32), this thesis/dissertation adheres to the provisions of Purdue University's "Policy of Integrity in Research" and the use of copyright material.

Approved by Major Professor(s): Wenbin Yu

Approved by: Weinong Wayne Chen 12/2/2016

Head of the Departmental Graduate Program Date

ANALYSIS OF COMPOSITE PLATES BY USING MECHANICS OF STRUCTURE GENOME AND COMPARISON WITH ANSYS

A Dissertation

Submitted to the Faculty

of

Purdue University

by

Banghua Zhao

In Partial Fulfillment of the

Requirements for the Degree

of

Master of Science in Aeronautics and Astronautics

December 2016

Purdue University

West Lafayette, Indiana

ACKNOWLEDGMENTS

First, I would like to thank my advisor Professor Wenbin Yu, who gave me the opportunity to join his group to do research and work with other group members. I learned a lot under his patient guidance and supervision. His teaching and research philosophy have a positive influence on my graduate study and career.

I would also like to thank my committee members, Professor Vikas Tomar and Professor Tyler Tallman, who have taken time from their busy schedule to attend my defense and have given variable suggestions to my thesis.

I would like to thank all the group members in Professor Wenbin Yu's group, who were always willing to help me when I was in trouble. I gained a lot of knowledge and experience by communication and interacting with them.

Last but not least, I would give thanks to my parents, who funded me to study abroad in America. Their endless love always cheers me up during my hard time.

TABLE OF CONTENTS

Page

LIST OF TABLES

LIST OF FIGURES

Figure Page

ABSTRACT

Zhao, Banghua MSAA, Purdue University, December 2016. Analysis of Composite Plates by Using Mechanics of Structure Genome and Comparison with ANSYS. Major Professor: Wenbin Yu.

Motivated by a recently discovered concept, Structure Genome (SG) which is defined as the smallest mathematical building block of a structure, a new approach named Mechanics of Structure Genome (MSG) to model and analyze composite plates is introduced. MSG is implemented in a general-purpose code named SwiftComp$^{\text{TM}}$, which provides the constitutive models needed in structural analysis by homogenization and pointwise local fields by dehomogenization. To improve the user friendliness of SwiftComp$^{\text{TM}}$, a simple graphic user interface (GUI) based on ANSYS Mechanical APDL platform, called ANSYS-SwiftComp GUI is developed, which provides a convenient way to create some common SG models or arbitrary customized SG models in ANSYS and invoke SwiftComp$^{\text{TM}}$ to perform homogenization and dehomogenization. The global structural analysis can also be handled in ANSYS after homogenization, which could predict the global behavior and provide needed inputs for dehomogenization.

To demonstrate the accuracy and efficiency of the MSG approach, several numerical cases are studied and compared using both MSG and ANSYS. In the ANSYS approach, 3D solid element models (ANSYS 3D approach) are used as reference models and the 2D shell element models created by ANSYS Composite PrepPost (ACP approach) are compared with the MSG approach. The results of the MSG approach agree well with the ANSYS 3D approach while being as efficient as the ACP approach. Therefore, the MSG approach provides an efficient and accurate new way to model composite plates.

1. INTRODUCTION

1.1 Motivation

Composite plates are widely used in many fields of industry ranging from civil to aerospace due to its lightness characteristics and high stiffness. The simplest composite plate could be composite laminates which are stacked up by layers with different materials or fiber orientations. Theoretically, one can use 3D elasticity theory to analyze composite plates. With the help of a commercial finite element software, one can use solid elements to build the corresponding 3D models to carry out the analysis. However, since composites are heterogeneous and anisotropic, insurmountable of degrees of freedom (DOFs) are needed to build a fine enough 3D finite element model. It costs tremendous computational power and time for engineers. The 3D approach is thus not practical and realistic. Alternatively, one can use various equivalent single layer (ESL) plate theories available in literature to carry out analysis. And many commercial finite element software codes provide the corresponding shell elements, which implement these theories. For example, ANSYS has linear 4-node SHELL181 element and quadratic 8-node SHELL281 element in their element database. Both of them are based on the first-order shear deformation theory (FSDT) [1].

However, while being computationally efficient, shell elements provided in commercial finite element software codes have many limitations. The major reason is that there are many ad hoc assumptions in ESL plate theories. Although these assumptions are commonly used by shell elements, many users are not aware of that. They may think that these shell elements capture the true characteristics of the structure. Nevertheless, it is not true in some circumstances. For example, in FSDT, the transverse normal stress is always zero as a direct result of the invoked ad hoc assumptions. However, this stress component is not zero in general if there is transverse load and

is very important for some failure criteria. Thus we need new approaches to analyze composite plates while being efficient and accurate.

1.2 Lecture Review

Since shell elements provided in commercial finite element software are based on ESL plate theories, the lecture review will mainly focus on ESL plate theories.

1.2.1 Equivalent Single Layer Plate Theories

The ESL plate theories are derived from the three-dimensional (3D) elasticity theory by making ad hoc assumptions with respect to the deformation or the stress state through the thickness of a composite plate. These assumptions allow the reduction of a 3D problem to a two-dimensional (2D) problem.

The simplest ESL plate theory is the classical laminated plate theory (CLPT), which is an extension of the Kirchhoff-Love plate theory to laminated composite plates. CLPT is based on two sets of assumptions: plane stress assumption and kinematic assumptions (also called Kirchhoff assumptions). The plane stress assumption states that the transverse stress components vanish for each layer of the composite laminate. The kinematic assumptions state that the transverse normal to the reference surface remains rigid, straight and normal. With these two sets of assumptions, the original 3D elasticity problem can be reduced to be a 2D problem. CLPT provides a reasonable prediction to thin laminates with the in-plane dimensions 20 times or more larger than the thickness. However, the two sets of ad hoc assumptions in CLPT create a contradiction: the zero transverse normal strain due to the Kirchhoff assumptions contradicts with the plane stress assumption unless the Poisson's ratio is zero. Besides, CLPT loses accuracy quickly if a laminate is thick and under transverse load. Thus more refined laminated plate theories are needed to better capture the response characteristics of composite plates.

The elimination of the transverse normal remaining normal assumption in CLPT leads to the first-order shear deformation theory (FSDT), which is also called the Reissner-Mindlin plate theory. Mindlin proposed his plate theory in 1951 [2] while a similar, but not identical plate theory had been proposed by Reissner [3] in 1945. Mindlin's theory assumes that there is a linear variation of displacement across the plate thickness whereas Reissner's theory assumes that the bending stress is linear while the shear stress is quadratic through the thickness of the plate. Both theories include transverse shear strains and both are extensions of Kirchhoff-Love plate theory including transverse shear effects. Since FSDT implies a linear displacement variation through the thickness, it is incompatible with Reissner's plate theory. But we still call FSDT as the Reissner-Mindlin plate theory because both share the same 2D plate model. A direct result of FSDT is that the transverse shear strain is constant through thickness and it needs shear correction factors to approximate the fact that transverse shear stress may be quadratic through thickness due to boundary conditions on the top and bottom surfaces [4]. The limitations of FSDT will be discussed in detail in Chapter 3. Nevertheless, in practical, FSDT is often adopted by commercial finite element software such as ANSYS due to its efficiency and relative accuracy than CLPT.

The higher-order shear deformation theory (HSDT) uses higher-order polynomials (second order or higher) for displacement through the thickness of a laminate. A famous one is the third-order laminated plated theory by Reddy [5]. The displacement field can provide quadratic variation of transverse shear strains and stresses for a general laminate composed of monoclinic layers. Thus there is no need to use shear correction factors. The third-order theory provides a slight increase in accuracy relative to FSDT, at the expense of an increase in computational effort. However, HSDT still assumes a displacement field a priori.

In 1979, Berdichevsky [6] first introduced the Variational Asymptotic Method (VAM) to analyze shells without involving ad hoc assumptions. VAM takes advantage of the small terms h/l, where h is the thickness and l is the characteristic length of

the reference surface of a composite plate, by dropping them from energy functional of 3D elasticity theory for different approximations, through which the 2D model is obtained. Thus, VAM provides a more systematic and mathematical justified way than traditional methods which use ad hoc assumptions. VAM was firstly extended to model composite plates by Atilgan and Hodges [7] in 1992. Their work was continued by Sutyrin and Hodges in [8] resulting in a Reissner-Mindlin-like model. Yu et al. [9–11] continued and extended their work to shells and developed a general Reissner-Mindlin-like model with accurate strain recovery and transverse normal stress. The resulting model was implemented by Yu [10, 12] by a finite element code named Variational Asymptotic Plate And Shell Analysis (VAPAS).

Recently, Yu [13] developed mechanics of structure genome (MSG) as a unified approach for composite modeling. MSG uses the VAM to avoid ad hoc assumptions and principle of minimum information loss (PMIL) to minimize information loss between the original model and the final macroscopic structural model. MSG is implemented into a general purpose code named SwiftComp$^{\text{TM}}$, which reproduces the capabilities of Variational Asymptotic Beam Section Analysis (VABS) [10, 14], VAPAS [10, 12], Variational Asymptotic Method for Unit Cell Homogenization (VAMUCH) [15] and many more capabilities not available in the previous three codes. It has been shown that MSG can be used to provide an efficient and accurate approach for composite beams [16] and a general-purpose solution for the free-edge stress problem [17]. It is the objective of this thesis to shown that MSG can be used for efficient high-fidelity modeling of composite plates.

1.2.2 Analysis of Composite Plates by ANSYS

ANSYS, Inc is a computer-aided engineering software provider. Their products include general-purpose FEA packages for numerically solving a wide variety of mechanical problems. For structural analysis, ANSYS Mechanical can solve linear or nonlinear static or dynamic problems. ANSYS FEA software is used throughout

industry to enable engineers to optimize their product designs. This thesis uses ANSYS to create reference models and comparison models. So a brief introduction about ANSYS capability and functionality to model composite structures is given below.

In general, ANSYS cam model composite structures by solid element, solid shell element and shell element. For simplification, this thesis does not use solid shell element. In addition, ANSYS provides ANSYS Composite PrepPost (ACP) to facilitate building finite element models (FEMs) and access results. So we will first introduce solid and shell elements, and then ACP.

For solid elements, ANSYS provides 8-node structural solid SOLID185 and 20-node structural solid SOLID186. Both of them are based on 3D Cauchy continuum model with three degrees of freedom at each node: translations in the nodal x, y, and z directions. SOLID185 is a linear element whereas SOLID186 is a quadratic serendipity element. If a composite structure has in-plane to thickness ratio not larger than 8, solid element is recommended.

For shell element, ANSYS provides 4-node structural shell SHELL181 and 8-node structural shell SHELL281. Both of them are based on FSDT with six degrees of freedom at each node: translations in the x, y, and z directions, and rotations about the x, y, and z-axes. SHELL181 is a linear element whereas SHELL281 is a quadratic serendipity element. If a composite structure has in-plane to thickness ratio larger than 8, shell element is recommended. Beside FSDT, many other technologies are used to improve the stress predictions within these shell element [1]. For example, ANSYS can obtain a linear varied transverse shear stress by set KEYOPT(8) equal to 1 or 2 if there is more than one layers. Also the transverse normal stress can be independently recovered during the element solution output from the applied pressure load. These technologies increase the accuracy of FSDT to some extent.

With those two types of elements and its powerful solver, ANSYS can easily solve composite structure problems as long as a model is set up. However, real composite plates could have very complex definitions that include numerous layers, materials, thicknesses and layup orientation. Without the proper FEA tools to set up a model,

one may spend too much time before one can actually get meaningful results. Even if the solution is done, it is very tedious to extract all the results needed such as the stress/strain field and failure index within every layer. To handle this problem, ANSYS Composite PrepPost (ACP) [18] is designed to perform preprocessing (build model) and postprocessing (extract solution) easier. ACP has a pre- and post-

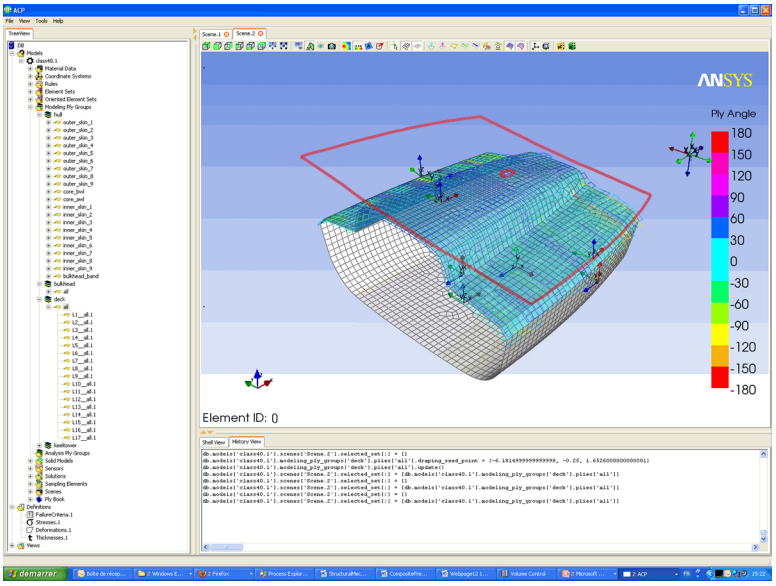

Figure 1.1. ANSYS Composite PrepPost

processing mode. In the pre-processing mode as shown in Figure 1.1, all composite definitions can be created and are mapped to the geometry (FE mesh). These composite definitions are transferred to the FE model and the solver input file. In the post-processing mode, after a completed solution and the import of the result files, post-processing results (failure, safety, strains and stresses) can be evaluated and visualized.

This thesis will use the powerful ACP preprocessing capabilities to easily build numerical cases, which will be called the ACP approach.

1.2.3 Present Work and Outline

The purpose of this thesis is to analyze composite plates using MSG and ANSYS and compare with ANSYS results. To use MSG and its corresponding code SwiftComp^{TM}, a graphical user interface (GUI) named ANSYS-SwiftComp GUI [19] is developed based on ANSYS platform for preprocessing and postprocessing needed for SwiftComp^{TM}. The global structural analysis is performed in ANSYS, which reads results from SwiftComp^{TM} homogenization and provides global behavior for SwiftComp^{TM} dehomogenization. The outline of the present work is followed.

Chapter 2 introduces the definition of MSG in detail. Different types of SG are explained for 3D structures, plates/shells and beams. The MSG-based multiscale modeling approach is explained at the end of the chapter.

Chapter 3 is divided into two sections. In the first section, FSDT is derived to provide a reference for the ACP approach and the limitation of FSDT is discussed. In the second section, the Reissner-Mindlin plate model based on VAM is derived so that the results in numerical cases can be better understood.

Chapter 4 presents five numerical cases to compare the MSG approach with the ANSYS 3D approach and the ACP approach for composite plate modeling. The results are discussed in detail, which reveals the accuracy and efficiency of MSG approach.

Chapter 5 concludes the present work and suggests possible improvements for future work.

2. MECHANICS OF STRUCTURE GENOME

This chapter provides an introduction to Mechanics of Structures Genome (MSG). MSG is the fundamental framework on which the new approach to analyze composite plates in this thesis is based. Hence, a brief introduction of MSG is presented in this chapter to set up the stage for the composite plate modeling using MSG in next chapter.

2.1 Introduction

In the field of biology, a genome is an organism's complete set of DNA, which contains all of the information needed to build and maintain that organism. Inspired by this concept, we can generalize the word genome to represent a fundamental building block of a system which is not biological. Then a new concept called the Structure Genome (SG) is defined as the smallest mathematical building block of a structure by Yu [13]. This definition represents an analogy between two different disciplines: SG containing all the constitutive information needed for a structure is similar to the genome containing all the genetic information for an organism's growth and development.

To understand the concept of SG, we need to carefully define the concept of structure first. Yu [20] clarified the distinction between structures and materials, which are often used interchangeably in literature. A structure is a solid body made of one or more materials with clearly defined interactions with its external environment through boundary conditions, applied loads, and environment effects, (*e.g.*, temperature and moisture) etc [21]. Despite the complexity of a structure, it can be modeled using one or more typical components as shown in Figure 2.1. If all three dimensions of a component are of similar size, it can be called a 3D structure; if one dimension

is much smaller than the other two dimensions, it can be called a plate/shell; if two dimensions are much smaller than the third dimension, it can be called a beam.

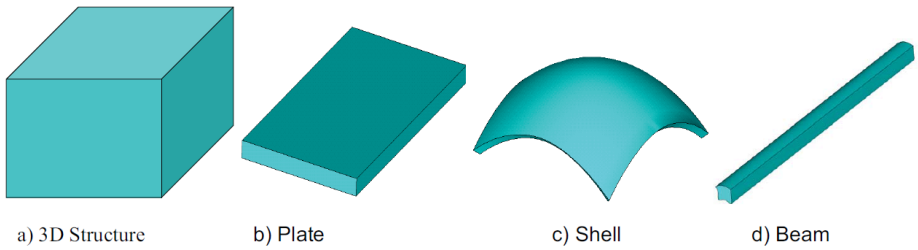

Figure 2.1. Typical structure components

Many models have been developed for these structural components. The classical ones are Cauchy elasticity for 3D structures, Kirchhoff-Love model for plates/shells, and Euler-Bernoulli model for beams. 3D structures can be considered as 3D models because the unknown functions are three-variable functions with three coordinates as independent variables. Plates/shells can be considered as 2D models because the unknowns functions are two-variable functions with two in-plane coordinates as independent variables. Beams can be considered as one-dimensional (1D) models because the unknowns functions are one-variable functions with the axial coordinate as the independent variable. To this end, beams/plates/shells can be collectively called dimensionally reducible structures as the models of these structural components are reduced from the original 3D model [10].

With the definition and categorization of structures in mind, we will then explain SG for 3D structures, SG for plates/shells and SG for beams in the following sections.

2.2 SG for 3D Structures

For 3D structures, SG is a generalization of the representative volume element (RVE) concept in micromechanics. As shown in Figure 2.2, depending on the heterogeneity of a 3D heterogeneous structure, a SG can be 1D, 2D or 3D. Also a SG

will use the lowest dimensions needed to represent the building block of the original structure.

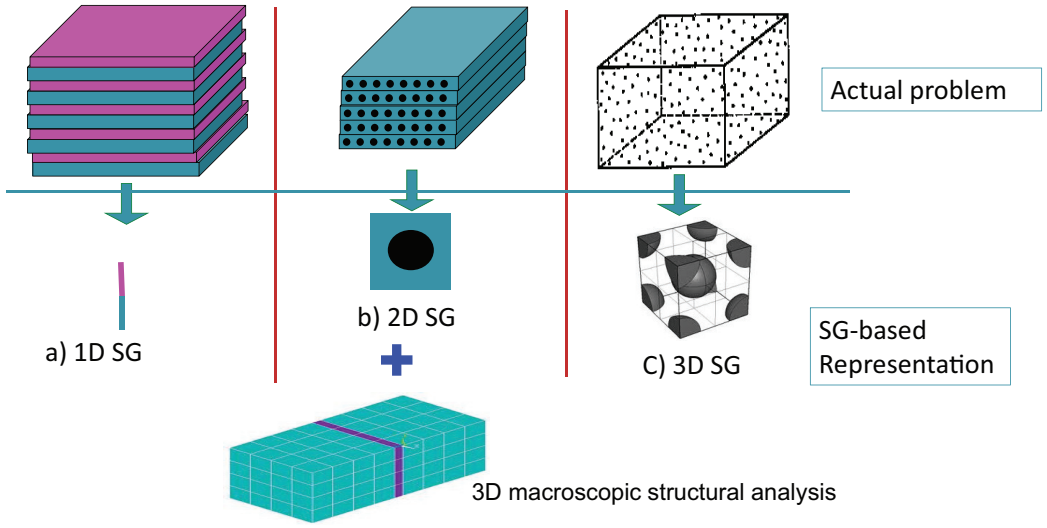

Figure 2.2. SG for 3D structures

For example, the binary composite in Figure 2.2a) features 1D heterogeneity, then a 1D SG with two different segments in corresponding to the two different phases can fully represent the original structure. Note we could also use 2D SG or 3D SG to represent this structure but it is unnecessary since 1D SG contains all the information we need for constitutive modeling. For 3D structures featuring 2D or 3D heterogeneity as shown in Figure 2.2b) and Figure 2.2c), the corresponding SG will be 2D or 3D.

After determining a SG, we can perform a homogenization analysis over the SG to obtain the constitutive models for the macroscopic structural analysis. For linear elastic behavior the constitutive information means the 6×6 effective stiffness matrix in the generalized Hooke's law. Then we can use this constitutive information to perform 3D macroscopic structural analyses as shown in the bottom of Figure 2.2. Finally, we can obtain the local fields of displacement/stress/strain of the SG in the original structure by dehomogenization. To this end, a 3D structure is considered as a 3D continuum and every material point of this continuum has an associated SG as its microstructure.

Thus, a SG has more features than RVE as summarized below:

- A 1D SG can be used to compute the complete set of 3D properties and local fields for structures with 1D heterogeneity. However, 1D RVE is not common and can not be used to compute the complete 3D properties and local fields.
- A 2D RVE only obtains in-plane properties and local fields. If the complete set of properties are needed for 3D structural analysis, a 3D RVE is usually required [22]. However, there is no such limitation in SG.
- Boundary conditions in terms of displacements and tractions indispensable in RVE-based models are not needed for SG-based models.
- Because SG-based models does not need to apply displacement or traction boundary conditions, MSG is more efficient than RVE analysis even for 3D SGs.

2.3 SG for Plates/Shells

For plate/shell structures, a SG can be 1D, 2D or 3D depending on the heterogeneity of the original structure as shown in Figure 2.3. The SGs we use in this thesis to analyze composite plates belong to this section. If a plate/shell features 1D heterogeneity as shown in Figure 2.3a), the SG is 1D. For plates/shells featuring 2D or 3D heterogeneity as shown in Figure 2.3b) and Figure 2.3c), the corresponding SG will be 2D or 3D.

Same as SG for 3D structures, 1D, 2D or 3D SG for plates/shells will give all constitutive information by homogenization and local fields of displacement/strain/stress by dehomogenization. And the constitutive information can be used directly for 2D plate/shell analysis as shown in the bottom of Figure 2.3. Here, however, the constitutive information means plate stiffness matrix, the 6×6 stiffness matrix for the Kirchhoff-Love plate model or the 8×8 stiffness matrix for the Reissner-Mindlin model. To this end, the reference surface of a plate/shell structure is considered as

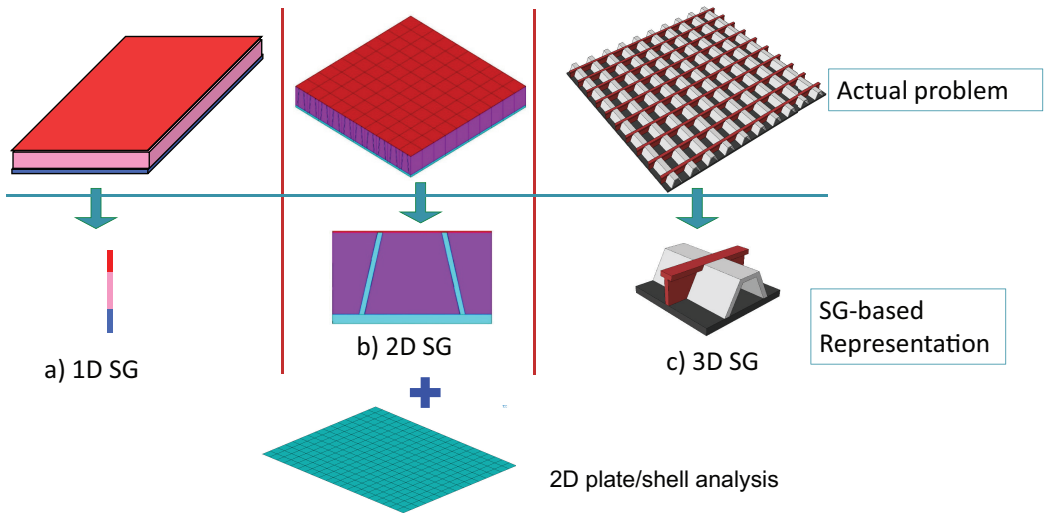

Figure 2.3. SG for Plates/Shells

a 2D continuum and every material point of this continuum has an associated SG as its microstructure.

This thesis will use 1D and 2D SGs to model plate/shell structures.

2.4 SG for Beams

For beam structures, a SG can be 2D or 3D depending on the heterogeneity of the original structure as shown in Figure 2.4. If a beam has uniform cross sections as shown in 2.4a), the SG is 2D. More specifically, it is a 2D cross-sectional domain. If the beam is also heterogeneous in the spanwise direction as shown in 2.4b), the SG will be 3D to represent the fundamental building block of the original beam structure.

Same as SG for 3D structures and plates/shells, 2D or 3D SG for beams will give all constitutive information by homogenization and local fields of displacement/strain/stress by dehomogenization. And the constitutive information can be used directly for 1D beam analysis as shown in the bottom of Figure 2.4. Here, however, the constitutive information means beam stiffness matrix, the 4×4 beam stiffness matrix for Euler-Bernoulli beam model or the 6×6 beam stiffness matrix for Timoshenko beam

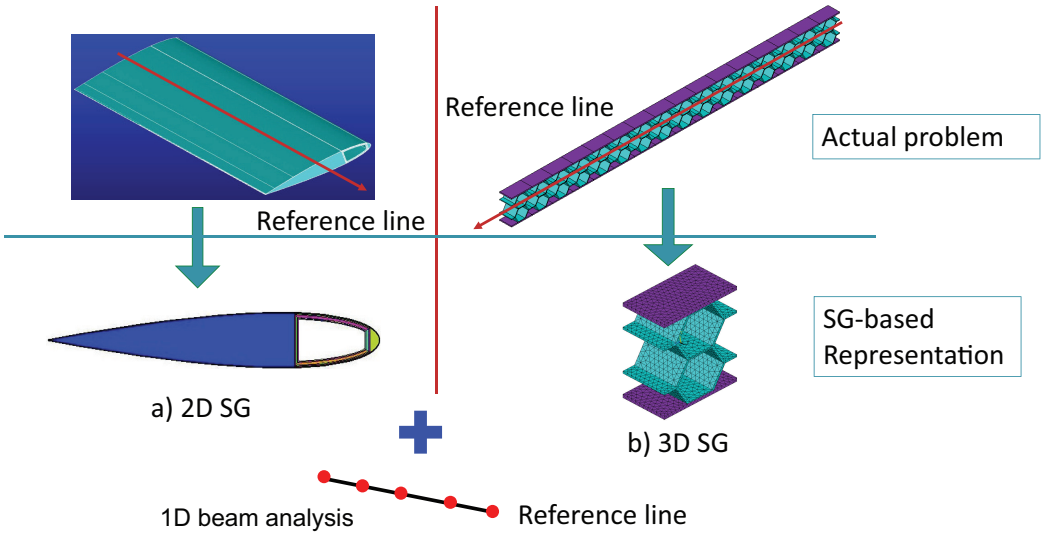

Figure 2.4. SG for Beams

model. To this end, the beam reference line of a beam structure is considered as a 1D continuum and every material point of this continuum has an associated SG as its microstructure.

2.5 MSG-based Multiscale Structural Modeling

Now we have clearly defined the meaning of SG. Then for different structures, MSG provides a rigorous and systematic approach to compute constitutive information (homogenization) and local fields (dehomogenization) within the original structures.

To use MSG approach practically, MSG-based multiscale structural modeling approach is introduced. It can be used to fill the gap between material genome and macroscopic structural analysis and can directly connect with simple structural elements (3D solid elements, plate/shell elements or beam elements) available in standard FEA software packages, such as shell elements in ANSYS.

The work flow of MSG is shown in Figure 2.5. First, MSG starts from the original model. Note the original model here means 3D continuum mechanics. Next, we identify SG based on the nature of original model and engineering experience. Then, MSG

uses the principle of minimum information loss (PMIL) based on the powerful variational asymptotic method (VAM) to decouple the original problem to a constitutive modeling over the SG and a structural analysis. The constitutive modeling has been implemented in a general-purpose software named SwiftComp^{TM}, which is developed by Professor Wenbin Yu at Purdue University. SwiftComp^{TM} can provide the constitutive models needed for the structural analysis by homogenization and pointwise local fields of displacement/strain/stress by dehomogenization. The global structural analysis could be easily handled by standard FEA software package such as ANSYS, which provides the global behavior for SwiftComp^{TM} to perform dehomogenization.

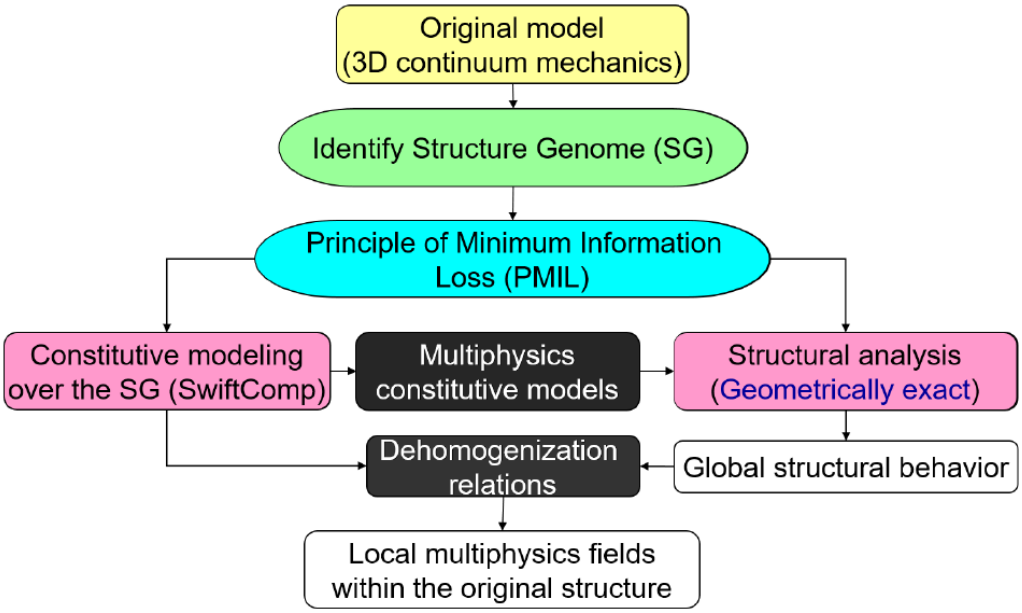

Figure 2.5. Work flow of Mechanics of Structure Genome

3. EQUIVALENT SINGLE LAYER PLATE THEORIES

The MSG in the above chapter is very general, which covers three major areas, i.e. 3D structures, plates/shells and beams. For a realistic scope, this thesis only considers a subset of MSG, i.e., plate-like structure for simplicity. In this chapter, the FSDT will be derived first to provide a reference for the ACP approach. The limitations of FSDT will be discussed in detail. Then the Reissner-Mindlin model based on VAM will be derived as a theory reference for the MSG approach. With these two derivations, the numerical cases in the next chapter can be better understood. Please note that all the derivations only reflect the author's understanding of the originally publication. All credits should go to the original authors [9, 10, 23, 24].

The sign convention of a composite plate is shown in Figure 3.1, which will be used in the rest of the thesis. Note, u_i and $\bar{u}_i$ are displacements and Φ_α are rotations. Greek indices represent in-plane values 1 and 2. Latin indices represent values 1, 2, and 3 in a 3D space. Repeated indices are summed over their range except where explicitly indicated.

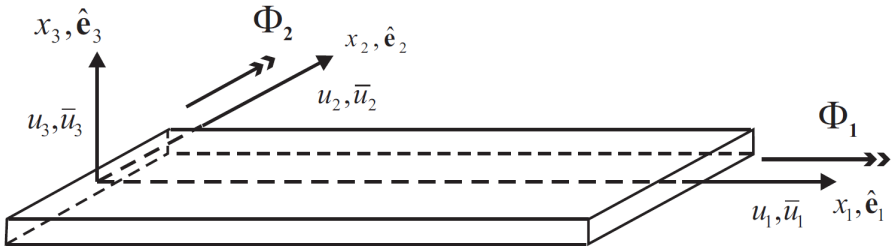

Figure 3.1. Sign convention for the displacements and rotation of a laminate

3.1 First Order Shear Deformation Theory

3.1.1 Kinematics

The kinematic assumptions of FSDT state that the transverse normal to the reference surface ($x_3 = 0$) remains rigid and straight, which implies the following displacement field within every material point of a composite plate. Note here, the kinematic assumptions are assumed a priori.

$$\begin{aligned} u_1(x_1, x_2, x_3) &= \bar{u}_1(x_1, x_2) + x_3\Phi_2(x_1, x_2) \\ u_2(x_1, x_2, x_3) &= \bar{u}_2(x_1, x_2) - x_3\Phi_1(x_1, x_2) \\ u_3(x_1, x_2, x_3) &= \bar{u}_3(x_1, x_2) \end{aligned} \tag{3.1}$$

where $\bar{u}_i$ and Φ_α are unknown functions as the displacements and rotations of material points on the reference surface.

The second assumption also implies the relationship between transverse shear strains to the slope of the reference surface and rotation of the transverse normal as depicted in Figure 3.2.

$$\begin{aligned} \gamma_{13} &= \bar{u}_{3,1} + \Phi_2 \\ \gamma_{23} &= \bar{u}_{3,2} - \Phi_1 \end{aligned} \tag{3.2}$$

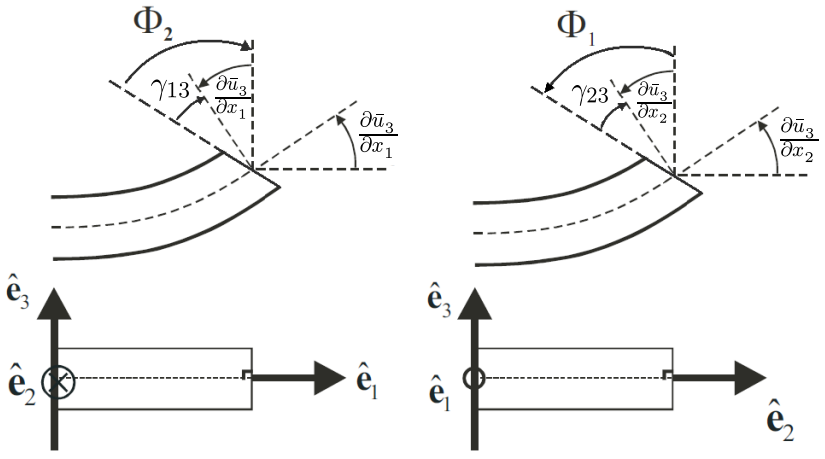

Figure 3.2. Plate reference surface slope and transverse normal

The infinitesimal strain defined in the 3D linear elasticity theory is.

$$\varepsilon_{ij} = \frac{1}{2}(u_{i,j} + u_{j,i}) \tag{3.3}$$

Substituting the displacement field in Eq. (3.1) into the definition of infinitesimal strain in Eq. (3.3), we get the 3D strain field within very material point of a composite plate.

$$\begin{aligned}
\varepsilon_{11}(x_1, x_2, x_3) &= \bar{u}_{1,1}(x_1, x_2) + x_3\Phi_{2,1}(x_1, x_2) \\
2\varepsilon_{12}(x_1, x_2, x_3) &= \bar{u}_{1,2}(x_1, x_2) + \bar{u}_{2,1}(x_1, x_2) + x_3[\Phi_{2,2}(x_1, x_2) - \Phi_{1,1}(x_1, x_2)] \\
\varepsilon_{22}(x_1, x_2, x_3) &= \bar{u}_{2,2}(x_1, x_2) - x_3\Phi_{1,2}(x_1, x_2) \\
2\varepsilon_{13}(x_1, x_2, x_3) &= \bar{u}_{3,1}(x_1, x_2) + \Phi_2(x_1, x_2) \\
2\varepsilon_{23}(x_1, x_2, x_3) &= \bar{u}_{3,2}(x_1, x_2) - \Phi_1(x_1, x_2) \\
\varepsilon_{33}(x_1, x_2, x_3) &= 0
\end{aligned} \tag{3.4}$$

Introducing 2D plate strain measures for FSDT

$$\begin{aligned}
\epsilon_{\alpha\beta} &= \frac{1}{2}(\bar{u}_{\alpha,\beta} + \bar{u}_{\beta,\alpha}) \\
\kappa_{11} = \bar{\Phi}_{2,1}, \quad \kappa_{22} &= -\bar{\Phi}_{1,2}, \quad \kappa_{12} = \frac{1}{2}[\bar{\Phi}_{2,2} - \bar{\Phi}_{1,1}]
\end{aligned} \tag{3.5}$$

Substituting 2D plate strain measures in Eqs. (3.5) and (3.2) into Eq. (3.4), we can express the 3D strain field in terms of 2D unknown plate strain measures as:

$$\begin{aligned}
\varepsilon_{\alpha\beta}(x_1, x_2, x_3) &= \epsilon_{\alpha\beta}(x_1, x_2) + x_3\kappa_{\alpha\beta}(x_1, x_2) \\
2\varepsilon_{\alpha3}(x_1, x_2, x_3) &= \gamma_{\alpha3}(x_1, x_2) \\
\varepsilon_{33}(x_1, x_2, x_3) &= 0
\end{aligned} \tag{3.6}$$

At this point, the original 3D strain fields are expressed in terms of 2D plate strains and the thickness coordinate x_3.

3.1.2 Constitutive Relations

In FSDT, we assume each layer is made of homogeneous monoclinic material and the transverse normal stress is equal to zero. The constitutive relation of each layer in 3D linear elasticity theory is:

$$\begin{Bmatrix} \varepsilon_e \\ 2\varepsilon_s \\ \varepsilon_t \end{Bmatrix} = \begin{bmatrix} S_e & 0 & S_{et} \\ 0 & S_s & 0 \\ S_{et}^{\mathrm{T}} & 0 & S_t \end{bmatrix} \begin{Bmatrix} \sigma_e \\ \sigma_s \\ \sigma_t \end{Bmatrix} \tag{3.7}$$

where

$$\varepsilon_e = \begin{Bmatrix} \varepsilon_{11} \\ \varepsilon_{22} \\ 2\varepsilon_{12} \end{Bmatrix} \qquad 2\varepsilon_s = \begin{Bmatrix} 2\varepsilon_{13} \\ 2\varepsilon_{23} \end{Bmatrix} \qquad \varepsilon_t = \Big\{ \varepsilon_{33} \Big\}$$

$$\sigma_e = \begin{Bmatrix} \sigma_{11} \\ \sigma_{22} \\ \sigma_{12} \end{Bmatrix} \qquad \sigma_s = \begin{Bmatrix} \sigma_{13} \\ \sigma_{23} \end{Bmatrix} \qquad \sigma_t = \Big\{ \sigma_{33} \Big\} = \Big\{ 0 \Big\}$$

$$S_e = \begin{bmatrix} S_{11} & S_{12} & S_{16} \\ S_{12} & S_{22} & S_{26} \\ S_{16} & S_{26} & S_{66} \end{bmatrix} \quad S_{et} = \begin{bmatrix} S_{13} \\ S_{23} \\ S_{36} \end{bmatrix} \quad S_s = \begin{bmatrix} S_{55} & S_{45} \\ S_{45} & S_{44} \end{bmatrix} \quad S_t = \Big[S_{33} \Big]$$

Eq. (3.7) implies the relationship between in-plane strains and in-plane stresses

$$\varepsilon_e = S_e \sigma_e \tag{3.8}$$

or the plane-stress reduced stress-strain relations

$$\sigma_e = Q \varepsilon_e \tag{3.9}$$

where the plane-stress reduced stiffness matrix $Q = S_e^{-1}$ depends on the material and orientation of a layer, which can be expressed explicitly as

$$Q = R_{\sigma e} Q' R_{\sigma e}^{\mathrm{T}} \tag{3.10}$$

where Q' is the plane-stress reduced stiffness matrix in the material coordinate system and $R_{\sigma e}$ is the in-plane stress transformation matrix for plane stress state, *i.e.*,

$$Q'^{-1} = S'_e = \begin{bmatrix} \frac{1}{E_1} & -\frac{\nu_{12}}{E_1} & \frac{\eta_{12,1}}{G_{12}} \\ -\frac{\nu_{12}}{E_1} & \frac{1}{E_2} & \frac{\eta_{12,2}}{G_{12}} \\ \frac{\eta_{12,1}}{G_{12}} & \frac{\eta_{12,2}}{G_{12}} & \frac{1}{G_{12}} \end{bmatrix} \qquad R_{\sigma e} = \begin{bmatrix} c^2 & s^2 & -2sc \\ s^2 & c^2 & 2sc \\ sc & -sc & c^2 - s^2 \end{bmatrix} \tag{3.11}$$

where $E_1, E_2, \nu_{12}, G_{12}, \eta_{12,1}, \eta_{12,2}$ are engineering constants of this layer in the material coordinate system. $c = \cos\theta, s = \sin\theta$ with θ denoting the layup angle.

The 3D constitutive relations in Eq. (3.7) also imply the relationship between transverse shear strains and transverse shear stresses as

$$2\varepsilon_s = S_s \sigma_s \tag{3.12}$$

where S_s is the transverse shear compliance matrix. The inverse relations are

$$\sigma_s = Q^*(2\varepsilon_s) \tag{3.13}$$

where the transverse shear stiffness matrix $Q^* = S_s^{-1}$ depends on the material and orientation of a layer, which can be expressed explicitly as

$$Q^* = \hat{R}_{\sigma s} Q^{*\prime} \hat{R}_{\sigma s}^{\mathrm{T}} \tag{3.14}$$

where $Q^{*\prime}$ is the transverse shear stiffness matrix in the material coordinate system and $\hat{R}_{\sigma s}$ is the transverse stress transformation matrix, *i.e.*,

$$Q^{*\prime -1} = S_s' = \begin{bmatrix} \frac{1}{G_{13}} & \frac{\mu_{23,13}}{G_{23}} \\ \frac{\mu_{23,13}}{G_{23}} & \frac{1}{G_{23}} \end{bmatrix} \qquad \hat{R}_{\sigma s} = \begin{bmatrix} c & -s \\ s & c \end{bmatrix} \tag{3.15}$$

where $G_{23}, G_{13}, \mu_{13,23}, \mu_{23,13}$ are engineering constants of this layer in the material coordinate system.

Eqs. (3.7) also implies that the transverse normal strain can be expressed as

$$\varepsilon_{33} = S_{et}^{\mathrm{T}} \sigma_e \tag{3.16}$$

Now, in order to express the 3D constitutive relations into its 2D counterpart, we introduce stress resultant $N_{\alpha\beta}, M_{\alpha\beta}$ and $N_{\alpha 3}$

$$\begin{aligned} N_{\alpha\beta} &= \langle \sigma_{\alpha\beta} \rangle \\ M_{\alpha\beta} &= \langle x_3 \sigma_{\alpha\beta} \rangle \\ \begin{Bmatrix} N_{13} \\ N_{23} \end{Bmatrix} &= K \begin{Bmatrix} \langle \sigma_{13} \rangle \\ \langle \sigma_{23} \rangle \end{Bmatrix} \end{aligned} \tag{3.17}$$

where

$$K = \begin{bmatrix} k_{11} & k_{12} \\ k_{12} & k_{22} \end{bmatrix} \tag{3.18}$$

where the angle brackets indicate piecewise integration through the thickness, that is $\langle \cdot \rangle = \sum_{i=1}^{N} \int_{z_i}^{z_{i+1}} \cdot dx_3$. $k_{\alpha\beta}$ are called the shear correction factors. Since transverse shear stresses vary at least parabolically through layer thickness if there is transverse force, shear correction factors are needed to approximate the true distribution of transverse shear stresses. In ANSYS, SHELL181 and SHELL281 element use an equivalent energy method to compute shear correction factors such that the strain energy due to transverse shear stress resultant is equal to the strain energy due to the true transverse shear stresses predicted by the 3D elasticity theory. These factors are predetermined based on the section lay-up at the start of solution [25]. The calculation of shear correction factors is given in Appendix A [26].

Substituting the 2D strain field in Eq. (3.6) into Eqs. (3.9) and (3.13), then into plate stress resultants in Eq. (3.17), we have 2D constitutive relations

$$\begin{Bmatrix} N \\ M \\ N^* \end{Bmatrix} = \begin{bmatrix} A & B & 0 \\ B & D & 0 \\ 0 & 0 & G \end{bmatrix} \begin{Bmatrix} \epsilon \\ \kappa \\ \gamma \end{Bmatrix} \tag{3.19}$$

where

$$N = \begin{Bmatrix} N_{11} \\ N_{22} \\ N_{12} \end{Bmatrix} \qquad M = \begin{Bmatrix} M_{11} \\ M_{22} \\ M_{12} \end{Bmatrix} \qquad N^* = \begin{Bmatrix} N_{13} \\ N_{23} \end{Bmatrix}$$

$$\epsilon = \begin{Bmatrix} \epsilon_{11} \\ \epsilon_{22} \\ 2\epsilon_{12} \end{Bmatrix} \qquad \kappa = \begin{Bmatrix} \kappa_{11} \\ \kappa_{22} \\ 2\kappa_{12} \end{Bmatrix} \qquad \gamma = \begin{Bmatrix} \gamma_{13} \\ \gamma_{23} \end{Bmatrix}$$

$$A = \langle Q \rangle \quad B = \langle x_3 Q \rangle \quad D = \langle x_3^2 Q \rangle \quad G = K \langle Q^* \rangle$$

At this point, the original 3D constitutive relations are reduced to 2D constitutive relations.

3.1.3 Equilibrium Equations

The equilibrium equations of FSDT will be derived by using the principle of virtual work

$$\delta U = \overline{\delta W} \tag{3.20}$$

Substitute 2D strain field in Eq. (3.6) into the virtual strain energy δU, we have

$$\begin{aligned}
\delta U &= \int_S \langle \sigma_{ij} \delta \varepsilon_{ij} \rangle dS = \int_S \langle \sigma_{\alpha\beta} \delta(\epsilon_{\alpha\beta} + x_3 \kappa_{\alpha\beta}) + \sigma_{\alpha 3} \delta \gamma_{\alpha 3} \rangle dS \\
&= \int_S (\langle \sigma_{\alpha\beta} \rangle \delta \epsilon_{\alpha\beta} + \langle x_3 \sigma_{\alpha\beta} \rangle \delta \kappa_{\alpha\beta} + \langle \sigma_{\alpha 3} \rangle \delta \gamma_{\alpha 3}) dS \\
&= \int_S [\frac{1}{2} N_{\alpha\beta} \delta(\bar{u}_{\alpha,\beta} + \bar{u}_{\beta,\alpha}) + M_{11} \delta \Phi_{2,1} - M_{22} \delta \Phi_{1,2} \\
&+ M_{12} \delta(\Phi_{2,2} - \Phi_{1,1}) + N_{13} \delta(\bar{u}_{3,1} + \Phi_2) + N_{23} \delta(\bar{u}_{3,2} - \Phi_1)] dS
\end{aligned} \tag{3.21}$$

where S denotes reference surface plane. Note the transverse shear stress resultants are defined as $N_{\alpha 3} = \langle \sigma_{\alpha 3} \rangle$ here. The shear correction factors are not introduced in the derivation of equilibrium equations.

Virtual work $\overline{\delta W}$ can be expressed as

$$\overline{\delta W} = \int_S \big(\langle f_i \delta u_i \rangle + \beta_i \delta u_i(x_1, x_2, -\frac{h}{2}) + \tau_i \delta u_i(x_1, x_2, \frac{h}{2}) \big) dS + \int_\Omega \langle t_i \delta u_i \rangle d\Omega \tag{3.22}$$

where f_i is distributed body force, τ_i, β_i and t_i are surface tractions on the top, bottom and lateral surfaces respectively. Ω denotes the boundary curve of the plate reference surface.

Substituting the 3D displacement field in Eq. (3.1) into virtual work in Eq. (3.22) we have

$$\overline{\delta W} = \int_S (p_i \delta \bar{u}_i + q_\alpha \delta \Phi_\alpha) dS + \int_\Omega (P_i \delta \bar{u}_i + Q_\alpha \delta \Phi_\alpha) d\Omega \tag{3.23}$$

Where $f_i, \beta_i, \tau_i, t_i, p_i, q_\alpha, P_i, Q_\alpha$ are defined by the equations below

$$\begin{aligned} p_i(x_1, x_2) &= \langle f_i \rangle + \beta_i + \tau_i \\ q_1(x_1, x_2) &= \frac{h}{2}(\beta_2 - \tau_2) - \langle x_3 f_2 \rangle \\ q_2(x_1, x_2) &= \frac{h}{2}(\tau_1 - \beta_1) + \langle x_3 f_1 \rangle \\ P_i &= \langle t_i \rangle \\ Q_1 &= -\langle x_3 t_2 \rangle \\ Q_2 &= \langle x_3 t_1 \rangle \end{aligned} \tag{3.24}$$

Substituting virtual strain energy δU in Eq. (3.21) and virtual work $\overline{\delta W}$ in Eq. (3.22) into the principle of virtual work in Eq. (3.20), we have

$$\begin{aligned} 0 = \int_S [&N_{11}\delta\bar{u}_{1,1} + N_{12}\delta\bar{u}_{1,2} + N_{12}\delta\bar{u}_{2,1} + N_{22}\delta\bar{u}_{2,2} + M_{11}\delta\Phi_{2,1} - M_{22}\delta\Phi_{1,2} \\ &- M_{12}\delta\Phi_{1,1} + M_{12}\delta\Phi_{2,2} + N_{13}\delta\bar{u}_{3,1} + N_{23}\delta\bar{u}_{3,2} + (N_{13} - q_2)\delta\Phi_2 \\ &- (N_{23} + q_1)\delta\Phi_1 - p_1\delta\bar{u}_1 - p_2\delta\bar{u}_2 - p_3\delta\bar{u}_3]dS \\ &- \int_\Omega (P_1\delta\bar{u}_1 + P_2\delta\bar{u}_2 + P_3\delta\bar{u}_3 + Q_1\delta\Phi_1 + Q_2\delta\Phi_2)d\Omega \end{aligned} \tag{3.25}$$

Integration by parts, we have

$$\begin{aligned} 0 = \int_S \big[&- (N_{11,1} + N_{12,2} + p_1)\delta\bar{u}_1 - (N_{12,1} + N_{22,2} + p_2)\delta\bar{u}_2 \\ &- (N_{13,1} + N_{23,2} + p_3)\delta\bar{u}_3 + (M_{12,1} + M_{22,2} - q_1 - N_{23})\delta\Phi_1 \\ &- (M_{11,1} + M_{12,2} + q_2 - N_{13})\delta\Phi_2\big]dS \\ &+ \int_\Omega \big[(n_1N_{11} + n_2N_{12} - P_1)\delta\bar{u}_1 + (n_1N_{12} + n_2N_{22} - P_2)\delta\bar{u}_2 \\ &+ (n_1N_{13} + n_2N_{23} - P_3)\delta\bar{u}_3 - (n_1M_{12} + n_2M_{22} + Q_1)\delta\Phi_1 \\ &+ (n_1M_{11} + n_2M_{12} - Q_2)\delta\Phi_2\big]d\Omega \end{aligned} \tag{3.26}$$

The 2D equilibrium equations correspond to the Euler-Lagrange equations in Eq. (3.26). Setting the coefficient before variations $\delta\bar{u}_i$ and $\delta\Phi_\alpha$ in the domain S to be zero will obtain:

$$\begin{aligned}
\delta\bar{u}_1: &\quad N_{11,1} + N_{12,2} + p_1 = 0 \\
\delta\bar{u}_2: &\quad N_{12,1} + N_{22,2} + p_2 = 0 \\
\delta\bar{u}_3: &\quad N_{13,1} + N_{23,2} + p_3 = 0 \\
\delta\Phi_1: &\quad M_{12,1} + M_{22,2} - q_1 - N_{23} = 0 \\
\delta\Phi_2: &\quad M_{11,1} + M_{12,2} + q_2 - N_{13} = 0
\end{aligned} \tag{3.27}$$

For boundary conditions, express displacements and rotations by normal and tangent components

$$\begin{aligned}
\delta\bar{u}_1 &= n_1\delta\bar{u}_n - n_2\delta\bar{u}_s \\
\delta\bar{u}_2 &= n_2\delta\bar{u}_n + n_1\delta\bar{u}_s \\
\delta\Phi_1 &= n_1\delta\Phi_n - n_2\delta\Phi_s \\
\delta\Phi_2 &= n_2\delta\Phi_n + n_1\delta\Phi_s
\end{aligned} \tag{3.28}$$

Then the boundary terms over domain Ω in Eq. (3.26) become

$$\begin{aligned}
0 = \int_\Omega [&(N_{nn} - P_n)\delta\bar{u}_n + (N_{ns} - P_s)\delta\bar{u}_s + (V_3 - P_3)\delta\bar{u}_3 \\
&- (M_{nn} - Q_n)\delta\Phi_n + (M_{ns} - Q_s)\delta\Phi_s]d\Omega
\end{aligned} \tag{3.29}$$

where

$$\begin{aligned}
N_{nn} &= n_1^2 N_{11} + n_2^2 N_{22} + 2n_1 n_2 N_{12} \\
N_{ns} &= n_1 n_2 (N_{22} - N_{11}) + (n_1^2 - n_2^2) N_{12} \\
P_n &= P_1 n_1 + P_2 n_2 \\
P_s &= -P_1 n_2 + P_2 n_1 \\
M_{nn} &= n_1 n_2 (M_{22} - M_{11}) + (n_1^2 - n_2^2) M_{12} \\
M_{ns} &= n_1^2 M_{11} + n_2^2 M_{22} + 2n_1 n_2 M_{12} \\
Q_n &= -Q_2 n_2 - Q_1 n_1 \\
Q_s &= Q_2 n_1 - Q_1 n_2 \\
V_3 &= n_1 N_{13} + n_2 N_{23}
\end{aligned} \tag{3.30}$$

Equation (3.29) implies that there are two sets of boundary conditions including displacement boundary conditions:

$$\bar{u}_n = u_n^0, \quad \bar{u}_s = u_s^0, \quad \bar{u}_3 = u_3^0, \quad \Phi_n = \Phi_n^0, \quad \Phi_s = \Phi_s^0 \qquad \text{on } \Omega_u \tag{3.31}$$

and force boundary conditions:

$$N_{nn} = P_n, \quad N_{ns} = P_s, \quad V_{n3} = P_3, \quad M_{nn} = Q_n, \quad M_{ns} = Q_s \qquad \text{on } \Omega_f \tag{3.32}$$

Here the portion of the boundary curve where the displacement is prescribed is denoted by Ω_u, and the portion of the boundary curve where the force is prescribed is denoted by Ω_f. And they have the relationship

$$\begin{aligned} \Omega_u \cap \Omega_f &= 0 \\ \Omega_u \cup \Omega_f &= \Omega \end{aligned} \tag{3.33}$$

3.1.4 Limitations

- As a direct result of kinematic assumptions, transverse normal strain ε_{33} is zero as shown in Eq. (3.6). This contradicts with the transverse normal stress assumption $\sigma_{33} = 0$ in Eq. (3.7) which results a nonzero transverse normal strain in Eq. (3.16) unless the Poison's ratio is zero. However, FSDT uses the strain field from kinematic assumptions along with $\sigma_{33} = 0$ in reduced stress-strain relations to derive 2D constitutive relations and equilibrium equations.
- The transverse stress results are not accurate. If there is transverse shear force, the transverse shear stress should be at least parabolic along the thickness whereas it is a constant in FSDT. Besides, the transverse normal stress is always zero by assumption. This directly ignores that fact that transverse normal stress exists if there is transverse load.
- The calculation of shear correction factors $k_{\alpha\beta}$ is tedious. There are many different formulas to calculate $k_{\alpha\beta}$ in literature. And the calculation of $k_{\alpha\beta}$ takes many factors into consideration such as the material and fiber orientation. The accuracy of transverse shear stress depends greatly on $k_{\alpha\beta}$.

3.2 The Reissner-Mindlin Plate Model Based on VAM

The ad hoc assumptions made by FSDT create many limitations as pointed out in the above section. However, the Reissner-Mindlin plate model based on VAM has no ad hoc assumptions as to be derived in the following. For simplicity, the following derivation only gives dimensional reduction up to the first order.

3.2.1 3D Formulation

The displacement within every material point of a composite plate can be expressed as

$$\begin{aligned} u_1(x_1, x_2, x_3) &= \bar{u}_1(x_1, x_2) - x_3\bar{u}_{3,1}(x_1, x_2) + w_1(x_1, x_2, x_3) \\ u_2(x_1, x_2, x_3) &= \bar{u}_2(x_1, x_2) - x_3\bar{u}_{3,2}(x_1, x_2) + w_2(x_1, x_2, x_3) \\ u_3(x_1, x_2, x_3) &= \bar{u}_3(x_1, x_2) + w_3(x_1, x_2, x_3) \end{aligned} \tag{3.34}$$

where w_i are unknown warping functions

With the introduction of warping functions, Eq. (3.34) can describe all the possible displacement within every material point of a composite plate. The kinematic assumptions of FSDT are equivalent to assume $w_i = 0$ and relaxing $\bar{u}_{3,1} = -\Phi_2,\ \bar{u}_{3,2} = \Phi_1$. Note unlike FSDT, there are no assumptions about the specific distribution of the displacement field through the thickness. The warping functions will be determined through the process of dimensional reduction described later. Let the origin of the thickness coordinate to be at the middle of the plate thickness. For a plate theory, the plate displacements $\bar{u}_i(x_1, x_2)$ can be defined as the average of 3D displacement through the thickness. i.e.,

$$h\bar{u}_i = \langle u_i \rangle \tag{3.35}$$

where h is the thickness of the composite plate. Eq. (3.35) implies the following constraints on the warping functions

$$\langle w_i \rangle = 0 \tag{3.36}$$

The 3D strain field is obtained by substituting Eq. (3.34) into the definition of infinitesimal strain in Eq. (3.3)

$$\begin{aligned}
\varepsilon_{11} &= \bar{u}_{1,1} - x_3\bar{u}_{2,11} + w_{1,1} \\
2\varepsilon_{12} &= \bar{u}_{1,2} + \bar{u}_{2,1} - 2x_3\bar{u}_{3,12} + w_{1,2} + w_{2,1} \\
\varepsilon_{22} &= \bar{u}_{2,2} - x_3\bar{u}_{1,22} + w_{2,2} \\
2\varepsilon_{13} &= w_{1,3} + w_{3,1} \\
2\varepsilon_{23} &= w_{2,3} + w_{3,2} \\
\varepsilon_{33} &= w_{3,3}
\end{aligned} \tag{3.37}$$

Introducing 2D strain measures as

$$\begin{aligned}
\epsilon_{\alpha\beta} &= \frac{1}{2}(\bar{u}_{\alpha,\beta} + \bar{u}_{\beta,\alpha}) \\
\kappa_{\alpha\beta} &= -\bar{u}_{3,\alpha\beta}
\end{aligned} \tag{3.38}$$

Note here $\kappa_{\alpha\beta}$ are different from the curvatures defined in FSDT (3.5). The curvatures here are the same as what defined in CLPT. They will be transferred to the Mindlin-Reissner model later.

Substituting Eq. (3.38) into Eq. (3.37). The 3D strain field can be expressed as:

$$\begin{aligned}
\varepsilon_e &= \epsilon + x_3\kappa + I_\alpha w_{\|,\alpha} \\
2\varepsilon_s &= {w_\|}' + e_\alpha w_{3,\alpha} \\
\varepsilon_t &= {w_3}'
\end{aligned} \tag{3.39}$$

where

$$\varepsilon_e = \begin{Bmatrix} \varepsilon_{11} \\ \varepsilon_{22} \\ 2\varepsilon_{12} \end{Bmatrix} \qquad 2\varepsilon_s = \begin{Bmatrix} 2\varepsilon_{13} \\ 2\varepsilon_{23} \end{Bmatrix} \qquad \varepsilon_t = \begin{Bmatrix} \varepsilon_{33} \end{Bmatrix}$$

$$\epsilon = \begin{Bmatrix} \epsilon_{11} \\ \epsilon_{22} \\ 2\epsilon_{12} \end{Bmatrix} \qquad \kappa = \begin{Bmatrix} \kappa_{11} \\ \kappa_{22} \\ 2\kappa_{12} \end{Bmatrix}$$

and

$$I_1 = \begin{bmatrix} 1 & 0 \\ 0 & 1 \\ 0 & 0 \end{bmatrix} \qquad I_2 = \begin{bmatrix} 0 & 0 \\ 1 & 0 \\ 0 & 1 \end{bmatrix} \qquad e_1 = \begin{Bmatrix} 1 \\ 0 \end{Bmatrix} \qquad e_2 = \begin{Bmatrix} 0 \\ 1 \end{Bmatrix}$$

Then, twice of the strain energy stored in a composite plate can be written as

$$2U = \int_S \left\langle \begin{Bmatrix} \varepsilon_e \\ 2\varepsilon_s \\ \varepsilon_t \end{Bmatrix}^{\mathrm{T}} \begin{bmatrix} C_e & C_{es} & C_{et} \\ C_{es}^{\mathrm{T}} & C_s & C_{st} \\ C_{et}^{\mathrm{T}} & C_{st}^{\mathrm{T}} & C_t \end{bmatrix} \begin{Bmatrix} \varepsilon_e \\ 2\varepsilon_s \\ \varepsilon_t \end{Bmatrix} \right\rangle dS = \int_S 2\mathcal{U} dS \tag{3.40}$$

Note, the material properties are general anisotropic.

For 3D virtual work done by applied loads, it can be written in two terms

$$\overline{\delta W} = \overline{\delta W}_{2D} + \overline{\delta W}^* \tag{3.41}$$

where

$$\overline{\delta W}_{2D} = \int_S (p_i \delta \bar{u}_i + q_1 \delta \bar{u}_{3,2} + q_2 \delta \bar{u}_{3,1}) dS + \int_\Omega (P_i \delta \bar{u}_i + Q_1 \delta \bar{u}_{3,2} + Q_2 \delta \bar{u}_{3,1}) d\Omega \tag{3.42}$$

$$\overline{\delta W}^* = \int_S (\langle f_i \delta w_i \rangle + \tau_i \delta w_i^+ + \beta_i \delta w_i^-) dS + \int_\Omega \langle t_i \delta w_i \rangle d\Omega \tag{3.43}$$

where $()^+ = ()|_{x_3=\frac{h}{2}}$, $()^- = ()|_{x_3=-\frac{h}{2}}$ and

$$\begin{aligned} p_i(x_1, x_2) &= \langle f_i \rangle + \beta_i + \tau_i \\ q_\alpha(x_1, x_2) &= \frac{h}{2}(\beta_\alpha - \tau_\alpha) - \langle x_3 f_\alpha \rangle \\ P_i &= \langle t_i \rangle \\ Q_\alpha &= -\langle x_3 t_\alpha \rangle \end{aligned} \tag{3.44}$$

Note the boundary line integral part of $\overline{\delta W}^*$ in Eq. (3.43) represents the work done through the virtual warping along the lateral boundary of a plate. This term is only for edge problem, which is beyond the scope of this thesis and will be dropped.

Now, according to the principal of virtual work in Eq. (3.20), we can construct the problem that has the warping functions as unknown functions to minimize total

potential energy density functional and $\overline{u}_i$ are not considered as variable functions. Note virtual work $\overline{\delta W}_{2D}$ is thus a constant term and will be dropped.

The total potential energy density is

$$\delta\Pi = 0 \qquad \text{with} \qquad \Pi = \mathcal{U} - \mathcal{W}^* \tag{3.45}$$

where

$$\overline{\delta W}^* = \delta \int_S \mathcal{W}^* dS \tag{3.46}$$

with

$$\mathcal{W}^* = \langle f_\parallel^{\mathrm{T}} w_\parallel \rangle + \langle f_3^{\mathrm{T}} w_3 \rangle + \tau_\parallel^{\mathrm{T}} w_\parallel^+ + \tau_3^{\mathrm{T}} w_3^+ + \beta_\parallel^{\mathrm{T}} w_\parallel^- + \beta_3^{\mathrm{T}} w_3^- \tag{3.47}$$

Now, VAM will be used to determine unknown warping functions asymptotically.

3.2.2 Dimensional Reduction

To use VAM, the first step is to assess the order of terms in the potential energy. Since a composite plate is a plate-like structure, the ratio of thickness to characteristic length of reference surface is inherently very small, i.e., $h/l \ll 1$. We will make use of this small term in dimensional reduction. Since the problem in consideration is a linear elastic problem, all the strains are assumed to be small. So we have $\varepsilon_{ij} \sim \epsilon_{\alpha\beta} \sim \epsilon$. The expressions of strains in Eq. (3.39) imply the order of curvature $h\kappa_{\alpha\beta} \sim \epsilon$. The order of strains implies that the order of warping function is either $w_i \sim h\epsilon$ or $w_i \sim l\epsilon$. However, if $w_i \sim l\epsilon$, then ε_{33} will be in the order of $(l/h)\epsilon$, which is much larger than ϵ. So the order of warping functions can only be $h\epsilon$. Then the orders of derivative of warping functions are

$$\begin{aligned} w_{\parallel,\alpha} &\sim w_{3,\alpha} \sim \frac{h}{l}\epsilon \\ w_\parallel{}' &\sim w_3{}' \sim \epsilon \end{aligned} \tag{3.48}$$

Consider the 2D plate equilibrium equation in Eqs. (3.27). The orders of surface traction are

$$\begin{aligned} hf_\alpha &\sim \tau_\alpha \sim \beta_\alpha \sim \mu\frac{h}{l}\epsilon \\ hf_3 &\sim \tau_3 \sim \beta_3 \sim \mu(\frac{h}{l})^2\epsilon \end{aligned} \tag{3.49}$$

where μ is the order of material properties.

Zeroth-Order Approximation

Now, the total potential energy density can be written explicitly as

$$\begin{aligned}2\Pi =&\langle\underline{\underline{(\epsilon+x_3\kappa)^{\mathrm{T}}C_e(\epsilon+x_3\kappa)}}+\underline{2(\epsilon+x_3\kappa)^{\mathrm{T}}C_eI_\alpha w_{\parallel,\alpha}}+\underline{2(I_\alpha w_{\parallel,\alpha})^{\mathrm{T}}C_eI_\alpha w_{\parallel,\alpha}}\\&+2(\epsilon+x_3\kappa)^{\mathrm{T}}C_{es}w_\parallel{}'+\underline{2(\epsilon+x_3\kappa)^{\mathrm{T}}C_{es}e_\alpha w_{3,\alpha}}+\underline{2(I_\alpha w_{\parallel,\alpha})^{\mathrm{T}}C_{es}(w_\parallel{}'+e_\alpha w_{3,\alpha})}\\&+2(\epsilon+x_3\kappa)^{\mathrm{T}}C_{et}w_3{}'+\underline{2(I_\alpha w_{\parallel,\alpha})^{\mathrm{T}}C_{et}w_3{}'}+w_\parallel{}'^{\mathrm{T}}C_sw_\parallel{}'+\underline{2w_\parallel{}'^{\mathrm{T}}C_se_\alpha w_{3,\alpha}}\\&+\underline{2(e_\alpha w_{3,\alpha})^{\mathrm{T}}C_se_\alpha w_{3,\alpha}}+2w_\parallel{}'^{\mathrm{T}}C_{st}w_3{}'+\underline{2(e_\alpha w_{3,\alpha})^{\mathrm{T}}C_{st}w_3{}'}+C_tw_3{}'^2\rangle\\&-\underline{2\big(\langle f_\parallel^{\mathrm{T}}w_\parallel\rangle+\langle f_3^{\mathrm{T}}w_3\rangle+\tau_\parallel^{\mathrm{T}}w_\parallel^{+}+\tau_3^{\mathrm{T}}w_3^{+}+\beta_\parallel^{\mathrm{T}}w_\parallel^{-}+\beta_3^{\mathrm{T}}w_3^{-}\big)}\end{aligned}\tag{3.50}$$

where the underlined terms are in the order of h/l or higher and are dropped in the zeroth-order approximation. The double underlined terms are constants which will not affect the stationary points and can be simply dropped.

Since the unknown warping functions are subjected to constraints, Lagrange multiplier method is used. Then the stationary conditions for the total potential energy density can be obtained from the following variational statement

$$\delta I=0\quad\text{with}\quad I=\Pi+\lambda_\parallel\langle w_\parallel\rangle+\lambda_3\langle w_3\rangle\tag{3.51}$$

Dropping the underlined and double underlined terms in Eq. (3.50) and leaving only the leading terms, the variation with respect to the warping functions of the zeroth-order variational statement is

$$\begin{aligned}\delta I_0=&\langle[(\epsilon+x_3\kappa)^{\mathrm{T}}C_{es}+w_\parallel{}'^{\mathrm{T}}C_s+w_3{}'C_{st}^{\mathrm{T}}]\delta w_\parallel{}'+\lambda_\parallel\delta w_\parallel\\&+[(\epsilon+x_3\kappa)^{\mathrm{T}}C_{et}+w_\parallel{}'^{\mathrm{T}}C_{st}+w_3{}'C_t]\delta w_3{}'+\lambda_3\delta w_3\rangle=0\end{aligned}\tag{3.52}$$

Integration by part, Eq. (3.52) yields the following Euler-Lagrange equations

$$\delta w_\parallel:\qquad[(\epsilon+x_3\kappa)^{\mathrm{T}}C_{es}+w_\parallel{}'^{\mathrm{T}}C_s+w_3{}'C_{st}^{\mathrm{T}}]'=\lambda_\parallel\tag{3.53}$$

$$\delta w_3:\qquad[(\epsilon+x_3\kappa)^{\mathrm{T}}C_{et}+w_\parallel{}'^{\mathrm{T}}C_{st}+w_3{}'C_t]'=\lambda_3\tag{3.54}$$

Since w_i are free to vary at top and bottom surfaces, δw_i may be not equal to zero. The boundary conditions from integration by part are

$$\begin{aligned} \delta w_{\|}: \qquad & [(\epsilon + x_3\kappa)^{\mathrm{T}} C_{es} + {w_{\|}}'^{\mathrm{T}} C_s + {w_3}' C_{st}^{\mathrm{T}}]^+ = 0 \\ & [(\epsilon + x_3\kappa)^{\mathrm{T}} C_{es} + {w_{\|}}'^{\mathrm{T}} C_s + {w_3}' C_{st}^{\mathrm{T}}]^- = 0 \end{aligned} \tag{3.55}$$

$$\begin{aligned} \delta w_3: \qquad & [(\epsilon + x_3\kappa)^{\mathrm{T}} C_{et} + {w_{\|}}'^{\mathrm{T}} C_{st} + {w_3}' C_t]^+ = 0 \\ & [(\epsilon + x_3\kappa)^{\mathrm{T}} C_{et} + {w_{\|}}'^{\mathrm{T}} C_{st} + {w_3}' C_t]^- = 0 \end{aligned} \tag{3.56}$$

Integrating Eq. (3.53) and Eq. (3.54) and substituting boundary conditions from Eqs. (3.55) and (3.56), we get $\lambda_{\|} = 0$, $\lambda_3 = 0$ and the Euler-Lagrange equations can be written as

$$\delta w_{\|}: \qquad (\epsilon + x_3\kappa)^{\mathrm{T}} C_{es} + {w_{\|}}'^{\mathrm{T}} C_s + {w_3}' C_{st}^{\mathrm{T}} = 0 \tag{3.57}$$

$$\delta w_3: \qquad (\epsilon + x_3\kappa)^{\mathrm{T}} C_{et} + {w_{\|}}'^{\mathrm{T}} C_{st} + {w_3}' C_t = 0 \tag{3.58}$$

These two equations are satisfied at every point of a composite plate. Solving for ${w_{\|}}'^{\mathrm{T}}$ and ${w_3}'$, we get

$$\begin{aligned} {w_{\|}}'^{\mathrm{T}} &= -(\epsilon + x_3\kappa)^{\mathrm{T}} C_{es}^* C_s^{-1} \\ {w_3}' &= -(\epsilon + x_3\kappa)^{\mathrm{T}} C_{et}^* C_t^{*-1} \end{aligned} \tag{3.59}$$

where

$$\begin{aligned} C_t^* &= C_t - C_{st}^{\mathrm{T}} C_s^{-1} C_{st} \\ C_{et}^* &= C_{et} - C_{es} C_s^{-1} C_{st} \\ C_{es}^* &= C_{es} - \frac{C_{et}^* C_{st}^{\mathrm{T}}}{C_t^*} \end{aligned} \tag{3.60}$$

Substituting the solution of warping functions in Eq. (3.59) back into total potential energy density in Eq. (3.50) and drop underlined small terms, one can obtain the total potential energy density asymptotically correct to the zeroth-order as

$$2\Pi_0 = \langle (\epsilon + x_3\kappa)^{\mathrm{T}} C_e^* (\epsilon + x_3\kappa) \rangle = \begin{Bmatrix} \epsilon \\ \kappa \end{Bmatrix}^{\mathrm{T}} \begin{bmatrix} A^* & B^* \\ B^{*\mathrm{T}} & D^* \end{bmatrix} \begin{Bmatrix} \epsilon \\ \kappa \end{Bmatrix} \tag{3.61}$$

where

$$\begin{aligned} C_e^* &= C_e - C_{es}^* C_s^{-1} C_{es}^{\mathrm{T}} - \frac{C_{et}^* C_{et}^{\mathrm{T}}}{C_t^*} \\ A^* &= \langle C_e^* \rangle \qquad B^* = \langle x_3 C_e^* \rangle \qquad D^* = \langle x_3^2 C_e^* \rangle \end{aligned} \tag{3.62}$$

The first approximation coincides with CLPT. However, the transverse strains are not zero and this procedure does not need ad hoc assumptions regarding the displacement field or stress field.

The strain field of the zeroth-order approximation can be calculated as

$$\begin{aligned} \varepsilon_e^0 =& \epsilon + x_3\kappa \\ 2\varepsilon_s^0 =& w_\parallel' \\ \varepsilon_t^0 =& {w_3}' \end{aligned} \tag{3.63}$$

The stress field of the zeroth-order approximation can be calculated as

$$\begin{aligned} \sigma_e^0 =& C_e^*(\epsilon + x_3\kappa) \\ 2\sigma_s^0 =& 0 \\ \sigma_t^0 =& 0 \end{aligned} \tag{3.64}$$

First-Order Approximation

In the zeroth-order approximation, the warping functions are in the order of $h(\frac{h}{l})^0\varepsilon$ and the total potential energy is in the order of $(hl^2)\mu(\frac{h}{l})^0\epsilon^2$. Perturb the warping functions to include first-order terms v_i, which is in the order of $h(\frac{h}{l})\varepsilon$ as expressed in Eq. (3.65). Continue this process to find first-order approximation. Now the order of total potential energy is expected to be $(hl^2)\mu(\frac{h}{l})^2\epsilon^2$. We will drop terms greater than order $(h)\mu(\frac{h}{l})^2\epsilon^2$ in total potential energy density.

$$\begin{aligned} w_\parallel =& w_\parallel^0 + v_\parallel \\ w_3 =& w_3^0 + v_3 \end{aligned} \tag{3.65}$$

Then the orders of derivative of the first-order terms are

$$\begin{aligned} v_{\parallel,\alpha} \sim v_{3,\alpha} \sim& (\frac{h}{l})^2\epsilon \\ {v_\parallel}' \sim {v_3}' \sim& \frac{h}{l}\epsilon \end{aligned} \tag{3.66}$$

The constraints on warping functions in Eqs. (3.36) lead to the constraints on the first-order terms

$$\langle v_i \rangle = 0 \tag{3.67}$$

Since in most engineering problems, a composite layer presents at most monoclinic material symmetry, we will assume that the layer is monoclinic. So C_{es} and C_{st} terms will vanish in the constitutive relations and the resulting zeroth-order terms become

$$\begin{aligned} w_{\|}^0 =& 0 \\ w_3^0 =& C_{\perp}\mathcal{E} \end{aligned} \tag{3.68}$$

where

$$C_{\perp}{}' = \begin{bmatrix} -\frac{C_{et}^{\mathrm{T}}}{C_t} & -x_3\frac{C_{et}^{\mathrm{T}}}{C_t} \end{bmatrix} \tag{3.69}$$

and

$$\mathcal{E} = \begin{bmatrix} \epsilon & \kappa \end{bmatrix}^{\mathrm{T}} \tag{3.70}$$

Now, the total potential energy density can be written explicitly as

$$\begin{aligned} 2\Pi =& \langle \underline{\underline{(\epsilon + x_3\kappa)^{\mathrm{T}} C_e (\epsilon + x_3\kappa)}} + 2(\epsilon + x_3\kappa)^{\mathrm{T}} C_e I_\alpha v_{\|,\alpha} + \underline{(I_\alpha v_{\|,\alpha})^{\mathrm{T}} C_e I_\alpha v_{\|,\alpha}} \\ &+ \underline{\underline{2(\epsilon + x_3\kappa)^{\mathrm{T}} C_{et} w_3^{0\prime}}} + 2(\epsilon + x_3\kappa)^{\mathrm{T}} C_{et} v_3{}' + 2(I_\alpha v_{\|,\alpha})^{\mathrm{T}} C_{et} w_3^{0\prime} \\ &+ \underline{2(I_\alpha v_{\|,\alpha})^{\mathrm{T}} C_{et} v_3{}'} + v_{\|}{}'^{\mathrm{T}} C_s v_{\|}{}' + 2 v_{\|}{}'^{\mathrm{T}} C_s e_\alpha w_{3,\alpha}^0 + \underline{2 v_{\|}{}'^{\mathrm{T}} C_s e_\alpha v_{3,\alpha}} \\ &+ \underline{\underline{(e_\alpha w_{3,\alpha}^0)^{\mathrm{T}} C_s e_\alpha w_{3,\alpha}^0}} + \underline{(e_\alpha w_{3,\alpha}^0)^{\mathrm{T}} C_s e_\alpha v_{3,\alpha}} + \underline{(e_\alpha v_{3,\alpha})^{\mathrm{T}} C_s e_\alpha v_{3,\alpha}} \\ &+ \underline{\underline{w_3^{0\prime\mathrm{T}} C_t w_3^{0\prime}}} + 2 w_3^{0\prime\mathrm{T}} C_t v_3{}' + v_3{}'^{\mathrm{T}} C_t v_3{}' \rangle - \underline{\underline{2\big(\langle f_i w_i^0 \rangle + \tau_i w_i^{0+} + \beta_i w_i^{0-}\big)}} \\ &- 2\big(\langle f_{\|}^{\mathrm{T}} v_{\|} \rangle + \underline{\langle f_3^{\mathrm{T}} v_3 \rangle} + \tau_{\|}^{\mathrm{T}} v_{\|}^+ + \underline{\tau_3^{\mathrm{T}} v_3^+} + \beta_{\|}^{\mathrm{T}} v_{\|}^- + \underline{\beta_3^{\mathrm{T}} v_3^-}\big) \end{aligned} \tag{3.71}$$

Dropping the underlined and double underlined terms in Eq. (3.71) and leaving only the leading terms, the variation with respect to warping functions of the first-order variational statement is

$$\begin{aligned} \delta I_1 =& \langle (\epsilon + x_3\kappa)^{\mathrm{T}} C_e^* I_\alpha \delta v_{\|,\alpha} + (v_{\|}{}' + e_\alpha C_{\perp}\mathcal{E}_{,\alpha})^{\mathrm{T}} C_s \delta v_{\|}{}' \\ &- f_{\|}^{\mathrm{T}} \delta v_{\|} + \lambda_{\|} \delta v_{\|} + v_3{}' C_t \delta v_3{}' + \lambda_3 \delta v_3 \rangle \\ &+ \tau_{\|}^{\mathrm{T}} \delta v_{\|}^+ + \beta_{\|}^{\mathrm{T}} \delta v_{\|}^- = 0 \end{aligned} \tag{3.72}$$

Using integration by parts, Eq. (3.72) yields the following Euler-Lagrange equations

$$\delta v_{\|}: \qquad [C_s({v_{\|}}' + e_\alpha C_\perp \mathcal{E}_{,\alpha})]' = {D_\alpha}'\mathcal{E}_{,\alpha} + g' + \lambda_{\|} \tag{3.73}$$

$$\delta v_3: \qquad ({v_3}'^{\mathrm{T}} C_t)' = \lambda_3 \tag{3.74}$$

where

$$\begin{aligned} {D_\alpha}' &= -I_\alpha^{\mathrm{T}} \begin{bmatrix} C_e^* & x_3 C_e^* \end{bmatrix} \\ g' &= -f_{\|} \end{aligned} \tag{3.75}$$

Since v_i are free to vary at top and bottom surfaces, δv_i may not equal to zero. The boundary conditions from integration by part are

$$\begin{aligned} \delta v_{\|}: \qquad & [C_s({v_{\|}}' + e_\alpha C_\perp \mathcal{E}_{,\alpha})]^+ = \tau_{\|} \\ & [C_s({v_{\|}}' + e_\alpha C_\perp \mathcal{E}_{,\alpha})]^- = -\beta_{\|} \end{aligned} \tag{3.76}$$

$$\begin{aligned} \delta v_3: \qquad & ({v_3}' C_t)^+ = 0 \\ & ({v_3}' C_t)^- = 0 \end{aligned} \tag{3.77}$$

Integrating Eq. (3.74) and substituting boundary conditions in Eq. (3.77), we get $\lambda_3 = 0$ and the Euler-Lagrange equation can be written as

$$\delta v_3: \qquad {v_3}' C_t = 0 \tag{3.78}$$

This equation is satisfied at every point of a composite plate. Solving for ${v_3}'$ by considering the constraints in Eq. (3.67), we get

$$v_3 = 0 \tag{3.79}$$

In order to solve $v_{\|}$, integrating Eq. (3.73) with respect to x_3

$$C_s({v_{\|}}' + e_\alpha C_\perp \mathcal{E}_{,\alpha}) = D_\alpha \mathcal{E}_{,\alpha} + g + \lambda_{\|} x_3 + \Lambda_{\|} \tag{3.80}$$

where $\Lambda_{\|}$ is an integration constant.

Substituting boundary conditions in Eq. (3.76), the Lagrange multipliers and integration constant can be solved to be

$$\begin{aligned} \lambda_{\|} &= \frac{1}{h}(\tau_{\|} + \beta_{\|} - D_\alpha^+ \mathcal{E}_{,\alpha} + D_\alpha^- \mathcal{E}_{,\alpha} - g^+ + g^-) \\ \Lambda_{\|} &= \frac{1}{2}(\tau_{\|} - \beta_{\|} - D_\alpha^+ \mathcal{E}_{,\alpha} - D_\alpha^- \mathcal{E}_{,\alpha} - g^+ - g^-) \end{aligned} \tag{3.81}$$

Substituting Eqs. (3.81) back into Eq. (3.80) and solving for $v_\parallel{}'$, we get

$$v_\parallel{}' = C_s^{-1} D_\alpha^* \mathcal{E}_{,\alpha} + C_s^{-1} g^* \tag{3.82}$$

where

$$\begin{aligned} D_\alpha^* =& D_\alpha - C_s e_\alpha C_\perp + \frac{x_3}{h} C_\alpha^\mp - \frac{1}{2} C_\alpha^\pm \\ g^* =& g + \frac{x_3}{h} g^\mp - \frac{1}{2} g^\pm + (\frac{x_3}{h} + \frac{1}{2})\tau_\parallel + (\frac{x_3}{h} - \frac{1}{2})\beta_\parallel \end{aligned} \tag{3.83}$$

with the notation $()^\pm = ()^+ + ()^-$ and $()^\mp = ()^- - ()^+$

Integrating Eq. (3.82) both side, we get the following first-order warping functions

$$v_\parallel = \overline{D}_\alpha \mathcal{E}_{,\alpha} + \overline{g} \tag{3.84}$$

where

$$\begin{aligned} \overline{D}_\alpha{}' =& C_s^{-1} D_\alpha^* \\ \langle \overline{D}_\alpha \rangle =& 0 \end{aligned} \tag{3.85}$$

and

$$\begin{aligned} \overline{g}' =& C_s^{-1} g^* \\ \langle \overline{g} \rangle =& 0 \end{aligned} \tag{3.86}$$

Substituting the solution of warping functions in Eq. (3.84) back into total potential energy density in Eq. (3.71) and dropping underlined small terms, one can obtain the total potential energy asymptotically correct to the first-order as

$$2\Pi_1 = \mathcal{E}^{\mathrm{T}} A \mathcal{E} + \mathcal{E}_{,1}^{\mathrm{T}} B \mathcal{E}_{,1} + 2\mathcal{E}_{,1}^{\mathrm{T}} C \mathcal{E}_{,2} + \mathcal{E}_{,2}^{\mathrm{T}} D \mathcal{E}_{,2} - 2\mathcal{E}^{\mathrm{T}} F \tag{3.87}$$

where

$$\begin{aligned} A =& \begin{bmatrix} A^* & B^* \\ B^{*\mathrm{T}} & D^* \end{bmatrix} \\ B =& \langle C_{s(11)} C_\perp^{\mathrm{T}} C_\perp + \overline{D}_1^{\mathrm{T}} D_1{}' + D_1^{*\mathrm{T}} e_1 C_\perp \rangle \\ C =& \langle C_{s(12)} C_\perp^{\mathrm{T}} C_\perp + \frac{1}{2}(\overline{D}_1^{\mathrm{T}} D_2{}' + D_1{}'^{\mathrm{T}} \overline{D}_2 + D_1^{*\mathrm{T}} e_2 C_\perp + C_\perp{}^{\mathrm{T}} e_1^{\mathrm{T}} D_2^*) \rangle \\ D =& \langle C_{s(22)} C_\perp^{\mathrm{T}} C_\perp + \overline{D}_2^{\mathrm{T}} D_2{}' + D_2^{*\mathrm{T}} e_2 C_\perp \rangle \\ F =& \tau_3 C_\perp^{+\mathrm{T}} + \beta_3 C_\perp^{-\mathrm{T}} + \langle f_3 C_\perp^{\mathrm{T}} \rangle \\ & + \frac{1}{2}(\langle C_\perp^{\mathrm{T}} e_\alpha^{\mathrm{T}} g_{,\alpha}^* + D_\alpha{}'^{\mathrm{T}} \overline{g}_{,\alpha} - \overline{D}_\alpha^{\mathrm{T}} f_{\parallel,\alpha} \rangle - \overline{D}_\alpha^{+\mathrm{T}} \tau_{\parallel,\alpha} - \overline{D}_\alpha^{-\mathrm{T}} \beta_{\parallel,\alpha}) \end{aligned} \tag{3.88}$$

and $(\alpha\beta)$ in the subscript indicates the α, β th element in the corresponding matrix. Note the quadratic terms associated with the applied loads are dropped because they are not functions of 2D generalized strain $\mathcal{E}$.

The strain field of the first-order approximation can be calculated as

$$\begin{aligned} \varepsilon_e^1 =& \epsilon + x_3\kappa \\ 2\varepsilon_s^1 =& {v_\parallel}' + e_\alpha w_{3,\alpha}^0 \\ \varepsilon_t^1 =& w_3^{0\prime} \end{aligned} \tag{3.89}$$

The stress field of the first-order approximation can be calculated as

$$\begin{aligned} \sigma_e^1 =& C_e^*(\varepsilon + x_3\kappa) \\ 2\sigma_s^1 =& (D_\alpha^* + C_s e_\alpha C_\perp)\mathcal{E}_{,\alpha} + g^* \\ \sigma_t^1 =& 0 \end{aligned} \tag{3.90}$$

3.2.3 Transformation to the Reissner-Mindlin Model

Now, for practical applications and to use the shell elements available in commercial finite element software such as ANSYS, Eq. (3.87) needs to be transformed to a model having the same form as the Reissner-Mindlin plate theory.

In order to transform into the Reissner-Mindlin model, the transverse shear strains are introduced

$$\gamma = \begin{bmatrix} 2\gamma_{13} & 2\gamma_{23} \end{bmatrix}^{\mathrm{T}} \tag{3.91}$$

The relationship between the 2D generalized strain of the Reissner-Mindlin model, $\mathcal{R}$, and those of the classical plate model, $\mathcal{E}$, can be written as [10]

$$\mathcal{E} = \mathcal{R} - \mathcal{D}_\alpha \gamma_{,\alpha} \tag{3.92}$$

where

$$\mathcal{D}_1 = \begin{bmatrix} 0 & 0 & 0 & 1 & 0 & 0 \\ 0 & 0 & 0 & 0 & 1 & 0 \end{bmatrix}^{\mathrm{T}} \qquad \mathcal{D}_2 = \begin{bmatrix} 0 & 0 & 0 & 0 & 1 & 0 \\ 0 & 0 & 0 & 0 & 0 & 1 \end{bmatrix}^{\mathrm{T}} \tag{3.93}$$

$$\mathcal{R} = \begin{bmatrix} \varepsilon_{11}^* & 2\varepsilon_{12}^* & \varepsilon_{22}^* & K_{11}^* & 2K_{12}^* & K_{22}^* \end{bmatrix}^{\mathrm{T}} \tag{3.94}$$

where the in-plane strains $\varepsilon^*_{\alpha\beta}$ and curvatures $K^*_{\alpha\beta}$ are the 2D strain measures in the Reissner-Mindlin model.

Substituting Eq. (3.92) back into Eq. (3.87) and neglecting higher-order terms, the total potential density asymptotically correct to the first-order in terms of Reissner-Mindlin strains can be expressed as

$$\begin{aligned} 2\Pi_1 =& \mathcal{R}^{\mathrm{T}} A \mathcal{R} - 2\mathcal{R}^{\mathrm{T}} A \mathcal{D}_2 \gamma_{,2} - 2\mathcal{R}^{\mathrm{T}} A \mathcal{D}_1 \gamma_{,1} \\ &+ \mathcal{R}^{\mathrm{T}}_{,1} B \mathcal{R}_{,1} + 2\mathcal{R}^{\mathrm{T}}_{,1} C \mathcal{R}_{,2} + \mathcal{R}^{\mathrm{T}}_{,2} D \mathcal{R}_{,2} - 2\mathcal{R}^{\mathrm{T}} F \end{aligned} \tag{3.95}$$

The total potential energy of the Reissner-Mindlin plate model has the form of

$$2\Pi_R = \mathcal{R}^{\mathrm{T}} A \mathcal{R} + \gamma^{\mathrm{T}} G \gamma - 2\mathcal{R}^{\mathrm{T}} F_{\mathcal{R}} - 2\gamma^{\mathrm{T}} F_\gamma \tag{3.96}$$

Further derivation is needed to eliminate the terms with partial derivatives of the 2D generalized strains of the Reissner-Mindlin model. From the equilibrium equations, we have

$$\begin{aligned} M_{11,1} + M_{12,2} - N_{13} + m_1 = 0 \\ M_{12,1} + M_{22,2} - N_{23} + m_2 = 0 \end{aligned} \tag{3.97}$$

where $m_1 = q_2$ and $m_2 = -q_1$.

In the Reissner-Mindlin model, it has

$$\begin{aligned} \begin{Bmatrix} N \\ M \end{Bmatrix} &= A\mathcal{R} - F_{\mathcal{R}} \\ \begin{Bmatrix} N_{13} \\ N_{23} \end{Bmatrix} &= G\gamma - F_\gamma \end{aligned} \tag{3.98}$$

Combining Eqs. (3.97) and (3.98) together, we have

$$G\gamma - F_\gamma = \mathcal{D}^{\mathrm{T}}_\alpha A \mathcal{R}_{,\alpha} - \mathcal{D}^{\mathrm{T}}_\alpha A F_{\mathcal{R},\alpha} + \begin{Bmatrix} m_1 \\ m_2 \end{Bmatrix} \tag{3.99}$$

Then the transverse strain can be solved as

$$\gamma = G^{-1} F_\gamma + G^{-1} \mathcal{D}^{\mathrm{T}}_\alpha A \mathcal{R}_{,\alpha} - \mathcal{D}^{\mathrm{T}}_\alpha A F_{\mathcal{R},\alpha} + G^{-1} \begin{Bmatrix} m_1 \\ m_2 \end{Bmatrix} \tag{3.100}$$

Substituting Eq. (3.100) back into Eq. (3.95) and dropping higher-order terms not related with 2D generalized strains, Eq. (3.95) can be rewritten as

$$2\Pi_R = \mathcal{R}^{\mathrm{T}} A \mathcal{R} + \gamma^{\mathrm{T}} G \gamma - 2\mathcal{R}^{\mathrm{T}} F + U^* \tag{3.101}$$

where

$$U^* = \mathcal{R}_{,1}^{\mathrm{T}} \overline{B} \mathcal{R}_{,1} + 2\mathcal{R}_{,1}^{\mathrm{T}} \overline{C} \mathcal{R}_{,2} + \mathcal{R}_{,2}^{\mathrm{T}} \overline{D} \mathcal{R}_{,2} \tag{3.102}$$

and

$$\begin{aligned} \overline{B} =& B + A\mathcal{D}_1 G^{-1} \mathcal{D}_1^{\mathrm{T}} A \\ \overline{C} =& C + A\mathcal{D}_1 G^{-1} \mathcal{D}_2^{\mathrm{T}} A \\ \overline{D} =& D + A\mathcal{D}_2 G^{-1} \mathcal{D}_2^{\mathrm{T}} A \end{aligned} \tag{3.103}$$

If we can drive U^* to be zero for any $\mathcal{R}$, then we have found an asymptotically correct Reissner-Mindlin plate model. This can be achieved by using optimization process such as the least square technique to solve the overdetermined system for the constants as done in [9]. By the optimization process, the best transverse shear stiffness matrix G can be obtained to complete the transformation to the Reissner-Mindlin plate model. There is no need for shear correction factors and the transverse shear stress can be accurately calculated. We can continue the dimensional reduction process to obtain second-order approximate, which is needed for accurately recovering transverse normal stress.

3.2.4 Advantages

- There are no ad hoc assumptions involved in the derivation, which is mathematically more rigorous. No contradictions are created as appeared in FSDT.

- The transverse stress can be accurately recovered in the second-order approximation. Mathematically, the accuracy of the second-order approximation is comparable to zigzag plate theories with transverse shear stress expressed as a second-order polynomials.

- Shear correction factors are not needed in the derivation of the VAM-based Reissner-Mindlin model. The transverse shear stiffness matrix G can be obtained by the transformation to the Reissner-Mindlin plate model.

4. NUMERICAL EXAMPLES

In this chapter, five numerical cases are provided to demonstrate the accuracy and efficiency of the MSG-based plate analysis approach. To assess the accuracy, the corresponding equivalent 3D finite element models created by ANSYS solid element (ANSYS 3D approach) are provided as reference. To evaluate the efficiency, the 2D models created by ANSYS Composite PrepPost (ACP approach) are provided as comparison.

The modeling framework of the MSG approach is shown in Figure 4.1. The detailed steps are explained below.

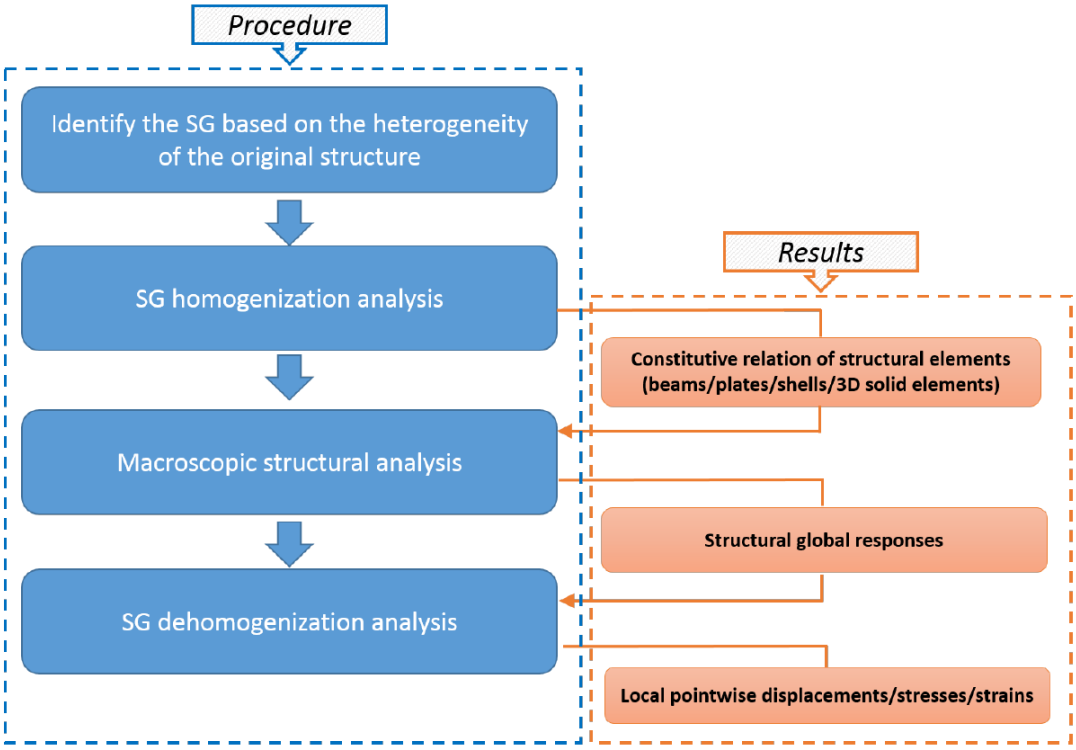

Figure 4.1. Modeling framework of the MSG approach

The first three cases will use 1D SG. The forth and fifth cases will use 2D SG. Having identified the SG, we will use SwiftComp$^{\text{TM}}$ to conduct SG homogenization analysis, whose input file, $*.sc$, is generated by ANSYS-SwiftComp GUI. Then we get the results of the homogenization analysis, $i.e$, A, B, D matrix. To get G matrix, VAPAS will be used instead. Note, in the current version of SwiftComp$^{\text{TM}}$, the Reissner-Mindlin model has not been included yet. So VAPAS will be used if the Reissner-Mindlin model is needed. In ANSYS, we can input A, B, D, G matrix directly into SHELL281 element for the macroscopic structural analysis. Then we obtain displacements for each node and 2D strain measures, i.e, $\epsilon_{\alpha\beta}$, $\kappa_{\alpha\beta}$ and $\gamma_{\alpha 3}$ for each element. Next, we identify the point we are interested in to recover local field. Note, we may need several nodes/elements around this point and use the finite difference method to get the derivative of 2D strain measures at this point in order to accurately recover the local field if we use VAPAS. Next, we will use SwiftComp$^{\text{TM}}$ again to perform dehomogenization analysis, whose input file, $*.glb$, is generated by ANSYS-SwiftComp GUI. Finally, we get the local pointwise distribution of displacements/stresses/strains over the SG.

For the ANSYS 3D approach, SOLID186 element will be used to create the reference model. Note, the ANSYS version used in all the cases is 17.1.

For the ACP approach, the geometry and layup information will be created in ANSYS Composite PrePost, which will generate the corresponding APDL files in ANSYS Workbench.

4.1 Case 1: A 6-layer Symmetric Thin Laminate

The first case is a [0/30/-30]s laminate. All the layers have same thickness of 0.01 inch. Each layer is assumed to be orthotropic. The lamina constants of the composites are $E_1 = 20 \times 10^6$ psi, $E_2 = E_3 = 1.45 \times 10^6$ psi, $G_{12} = G_{13} = 10^6$ psi, $G_{23} = 4.86577 \times 10^6$ psi, $\nu_{12} = \nu_{13} = 0.3$, $\nu_{23} = 0.49$. The geometry and boundary conditions are depicted in Figure 4.2. It is clamped at $x_1 = -0.5$ and subjected to a uniform pressure $P = 100$ psi at the top surface along the negative x_3 direction. The ratio of in-plane dimension to thickness is 16.67.

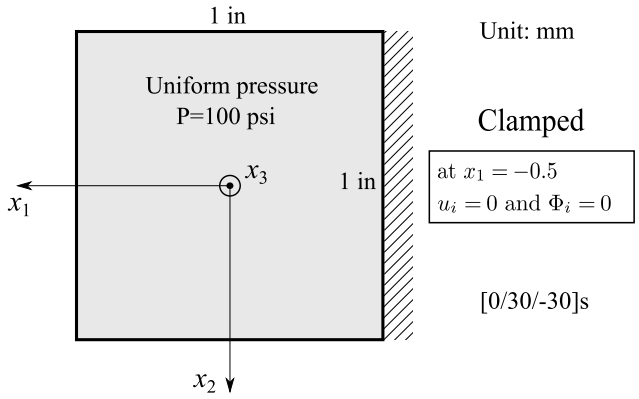

Figure 4.2. Geometry and boundary condition for case 1

The detailed steps for the MSG approach will be presented for case 1 as a demonstration. Other cases will follow a similar procedure and detailed steps are not repeated for simplicity.

First, the SG for case 1 is 1D. This 1D SG can be easily created in ANSYS-SwiftComp GUI. Click Preprocessor → Common SG → 1D SGs → Fast Generate. Then input Material number, Layup and Ply thickness for this laminate, i.e., 1, $'[0/30-30]s'$ and 0.01 respectively. For detailed instructions of creating a common SG, an introduction to ANSYS-SwiftComp GUI is given in Appendix B.

After creating 1D SG, the next step is to perform homogenization analysis to get A, B, D and G matrices of the laminate. Click Preprocessor $\rightarrow$ Solution $\rightarrow$ Homogenization $\rightarrow$ Plate/Shell Model. Keep default parameters and click OK. The effective properties will automatically pop up. Note, to get G matrix, VAPAS is used. The input file of SwiftComp$^{\text{TM}}$ can be easily modified to be the input files of VAPAS.

The third step is to perform global structural analysis. SHELL281 element is used to directly read A, B, D and G matrix. The mesh and boundary conditions are the same with the ACP approach. In order to input global behaviors for dehomogenization analysis, output the displacements values of a node at the center ($x_1 = 0,\ x_2 = 0$) as well as displacement values of 8 nodes neighboring to the center node. The 2D strain measures of 16 elements neighboring to the center node are also printed.

The last step is dehomogenization analysis. The finite difference method is used to get the global behaviors at the center node, if the dehomogenization is carried out by VAPAS, which needs the derivatives of 2D strain measures, i.e.,

$$\epsilon_{\alpha\beta,1},\ \kappa_{\alpha\beta,1},\ \epsilon_{\alpha\beta,2},\ \kappa_{\alpha\beta,2},\ \epsilon_{\alpha\beta,11},\ \kappa_{\alpha\beta,11},\ \epsilon_{\alpha\beta,12},\ \kappa_{\alpha\beta,12},\ \epsilon_{\alpha\beta,22},\ \kappa_{\alpha\beta,22}$$

In order to demonstrate the accuracy and efficiency of using the MSG approach, all the cases will also be analyzed by the ANSYS 3D approach and the ACP approach. Note, we will call the ANSYS 3D approach, the ACP approach and the MSG approach as ANSYS 3D, ACP and MSG respectively in all the cases for simplicity.

For case 1, ANSYS 3D has $614,400$ elements and $2,558,129$ nodes. There are 4 elements through the thickness of each layer. The reason that using such a fine mesh with approximately unity aspect ratio is to get the results converged so the model of ANSYS 3D can be treated as the reference. Both MSG and ACP have $25,600$ elements and $77,441$ nodes for the 2D plate analysis. In addition, MSG uses 6 more line elements with 25 nodes for MSG homogenization and dehomogenization analysis. The total number of elements and nodes of the three approaches are summarized in Table 4.1.

The displacement u_3 by the three approaches is shown in Figure 4.3. The displacement values are taken along a path from point $(-0.5, 0, 0)$ to point $(0.5, 0, 0)$.

Table 4.1 Finite element mesh information for case 1

Approach		**Element type**	**Elements**	**Nodes**
ANSYS 3D		SOLID186	614,400	2,558,129
ACP		SHELL281	25,600	77,441
MSG	SG	-	6	25
	2D Plate	SHELL281	25,600	77,441

As we can see, the displacement u_3 of both MSG and ACP agree well with ANSYS 3D.

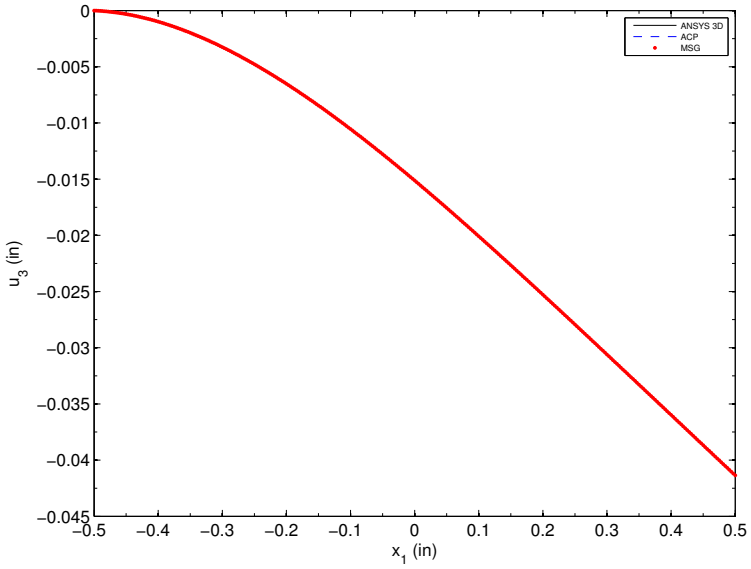

Figure 4.3. Comparison of deflection u_3 along x_1 at $x_2 = x_3 = 0$ for case 1

The stresses obtained from the three approaches are also compared. The stress values are taken through thickness at the center node ($x_1 = 0,\ x_2 = 0$). For ANSYS 3D, it is taken along a path from point $(0, 0, -0.03)$ to point $(0, 0, 0.03)$. For ACP, it is taken from data at TOP and BOTTOM for all layers. For MSG, the results are from dehomogenization.

For in-plane stresses, both MSG and ACP agree well with ANSYS 3D as shown from Figure 4.4 to Figure 4.6.

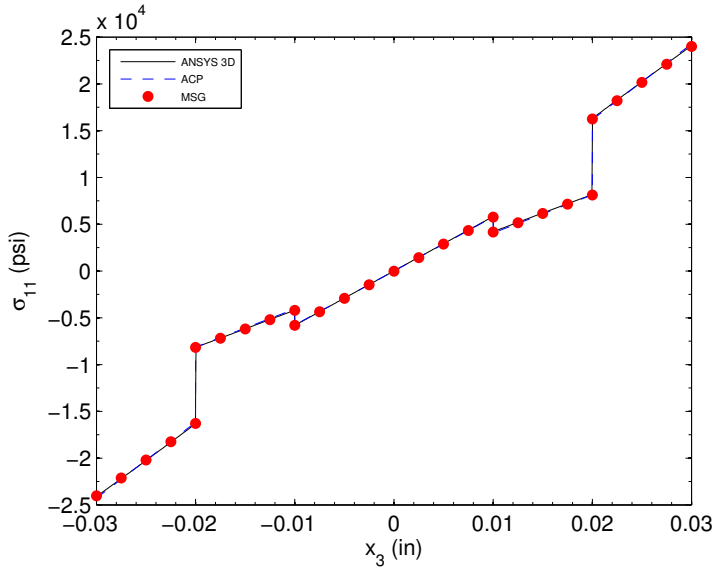

Figure 4.4. Comparison of stress σ_{11} through thickness for case 1

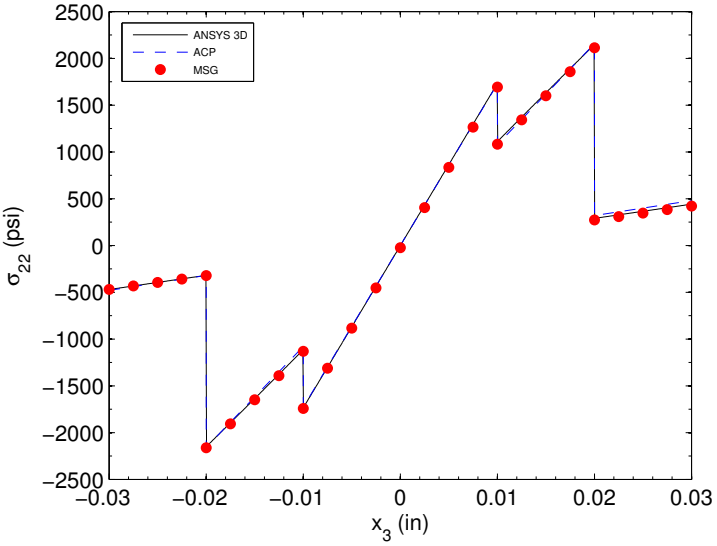

Figure 4.5. Comparison of stress σ_{22} through thickness for case 1

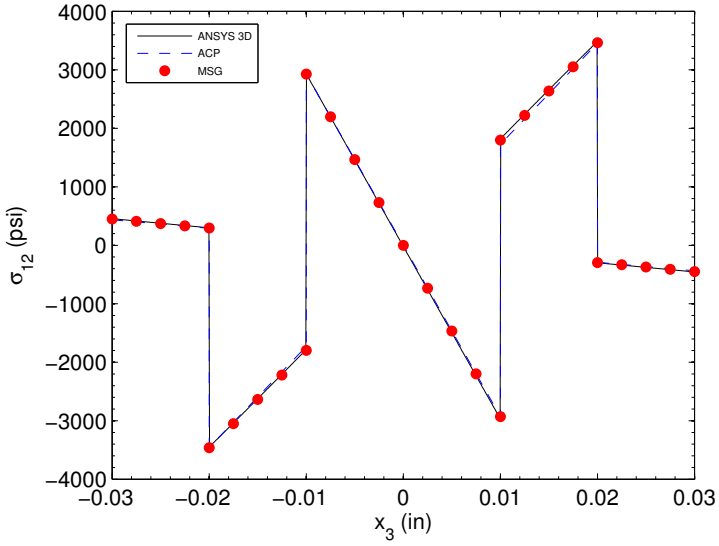

Figure 4.6. Comparison of stress σ_{12} through thickness for case 1

For transverse stresses, the MSG agrees well with ANSYS 3D while ACP loses accuracy as shown from Figure 4.7 to Figure 4.9.

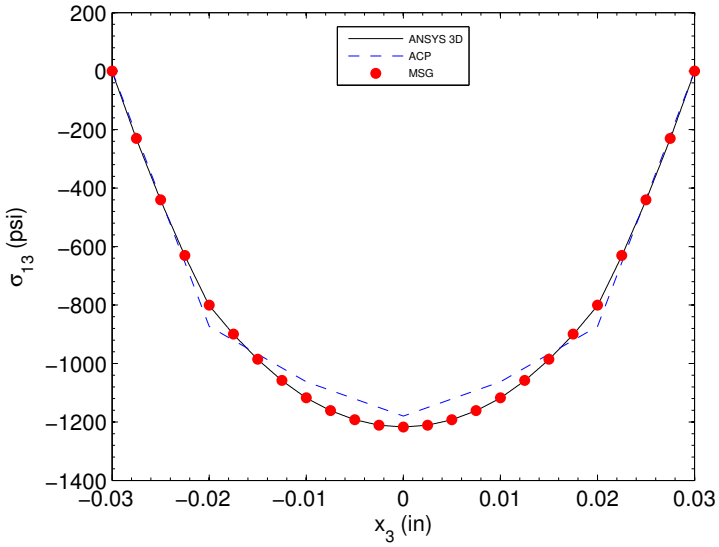

Figure 4.7. Comparison of stress σ_{13} through thickness for case 1

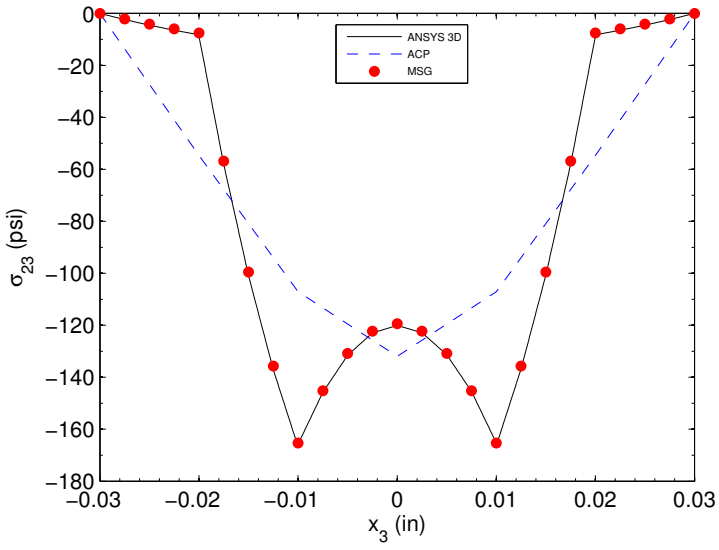

Figure 4.8. Comparison of stress σ_{23} through thickness for case 1

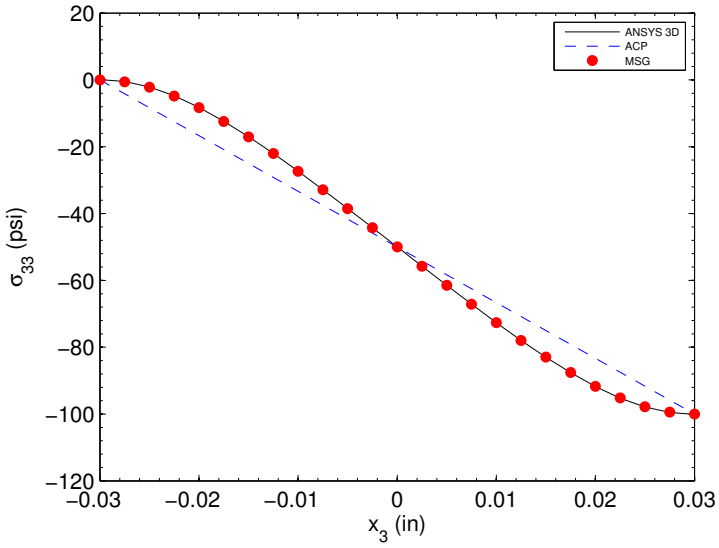

Figure 4.9. Comparison of stress σ_{33} through thickness for case 1

Specifically, the transverse shear stresses of ACP are piecewise linear while σ_{13} is quadratic and σ_{23} is more complex in ANSYS 3D. It is noted that ACP is a little bit better than FDST which only predicts a piecewise constant transverse shear stresses.

However, MSG is much better than ACP, which has a perfect match with ANSYS 3D. The transverse normal stress of ACP is linear through thickness while σ_{33} is at least second order polynomial in ANSYS 3D. Note, ACP is also better than FSDT since it can recover σ_{33} independently during the element solution output from the applied pressure load. Nevertheless, MSG is even better, which perfectly agrees with ANSYS 3D.

In terms of efficiency, the computation time among the three approaches are compared. It takes 3 hours and 44 seconds to build and solve the model by ANSYS 3D with 16 CPUs. For MSG, it takes less than 1 minute to build and solve the model with 2 CPUs. The comparison of computation time for the three approaches is listed in Table 4.2.

Table 4.2 Computation time for case 1

Approach		**CPUs**	**Time**	
ANSYS 3D		16	3 h 44 sec	
ACP		2	45 sec	
MSG	Homogenization	2	1 sec	34 sec
	Structural analysis	2	32 sec	
	Dehomogenization	2	1 sec	

It is clear that MSG is $2,551$ times more efficient than ANSYS 3D and is even slightly faster than ACP. The ACP is 11 seconds slower because of the time for calculation of shear correction factors.

4.2 Case 2: A 8-layer Unsymmetrical Thick Laminate

The second case is a [0/90/45/-45/30/-30/75/-75] laminate. All the layers have same thickness of 0.02 inch. Each layer is assumed to be orthotropic with material properties being the same as case 1. The geometry and boundary conditions are depicted in Figure 4.10. It is clamped at $x_1 = -0.5$ and subjected to point force $F_3 = -100$ lb at $(0.5, 0, 0)$. The ratio of in-plane dimension to thickness is 6.25.

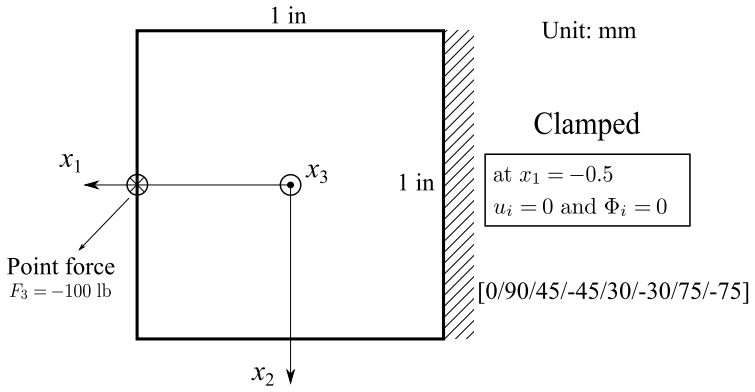

Figure 4.10. Geometry and boundary condition for case 2

The ANSYS 3D has $834,945$ elements and $3,385,026$ nodes. There are 4 elements through the thickness of each layer. Both MSG and ACP have $25,921$ elements and $77,442$ nodes for 2D plate analysis. In addition, MSG uses 8 more line elements with 33 nodes for MSG homogenization and dehomogenization analysis. The total number of elements and nodes of the three approaches are summarized in Table 4.3.

The displacement u_3 by the three approaches is shown in Figure 4.11. The displacement values are taken along a path from point $(-0.5, 0, 0)$ to point $(0.5, 0, 0)$. As we can see, the displacement u_3 of both MSG and ACP agree well with ANSYS 3D.

Table 4.3 Finite element mesh information for case 2

Approach		**Element type**	**Elements**	**Nodes**
ANSYS 3D		SOLID186	834,945	3,385,026
ACP		SHELL281	25,921	77,442
MSG	SG	-	8	33
	2D Plate	SHELL281	25,921	77,442

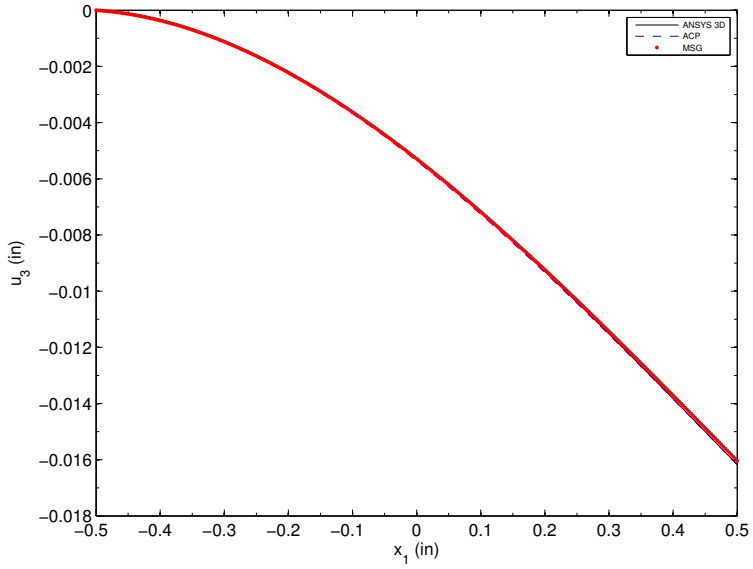

Figure 4.11. Comparison of deflection u_3 along x_1 at $x_2 = x_3 = 0$ for case 2

The stresses obtained from the three approaches are compared. The stress values are taken along thickness at the center node ($x_1 = 0,\ x_2 = 0$). For ANSYS 3D, it is taken along a path from point $(0, 0, -0.08)$ to point $(0, 0, 0.08)$.

For in-plane stress, both MSG and ACP agree well with ANSYS 3D as shown from Figure 4.12 to Figure 4.14.

For transverse stresses, the MSG agrees well with ANSYS 3D while ACP loses accuracy as shown from Figure 4.15 to Figure 4.17. The transverse shear stress σ_{13} of ACP agrees with ANSYS 3D but slightly worse than MSG. The transverse shear

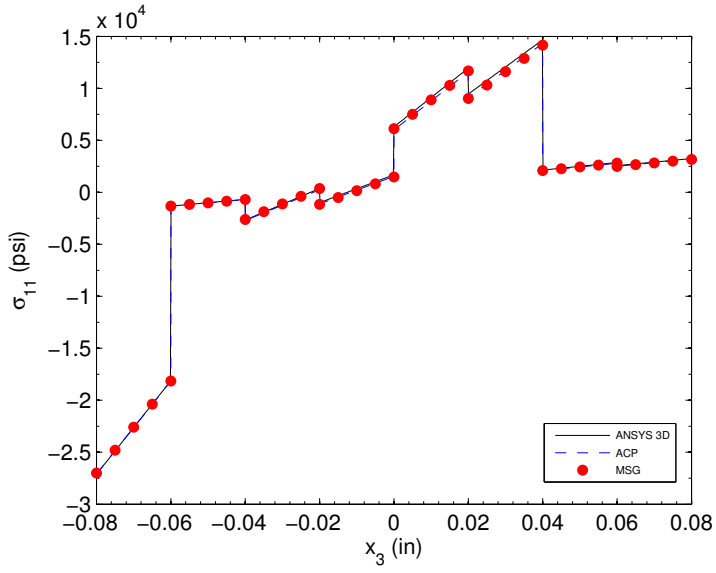

Figure 4.12. Comparison of stress σ_{11} through thickness for case 2

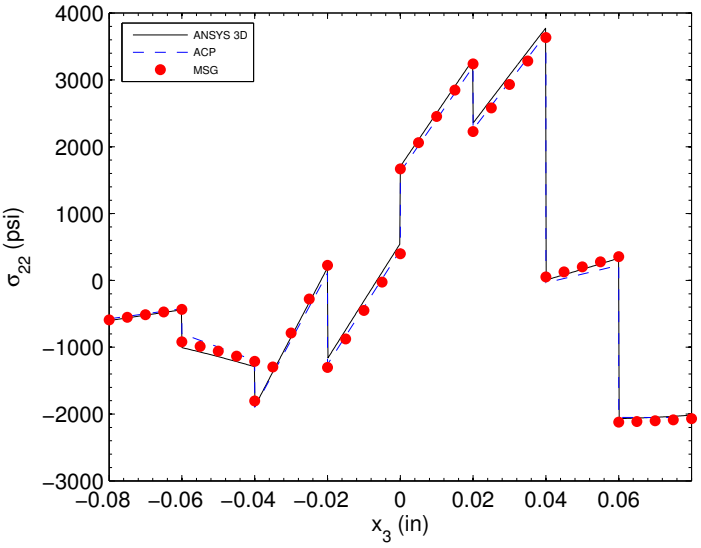

Figure 4.13. Comparison of stress σ_{22} through thickness for case 2

stress σ_{23} of ACP can not capture the variation of stress if $x_3 > -0.04$. The transverse normal stress of ACP is zero through thickness since there is no pressure applied to the laminate.

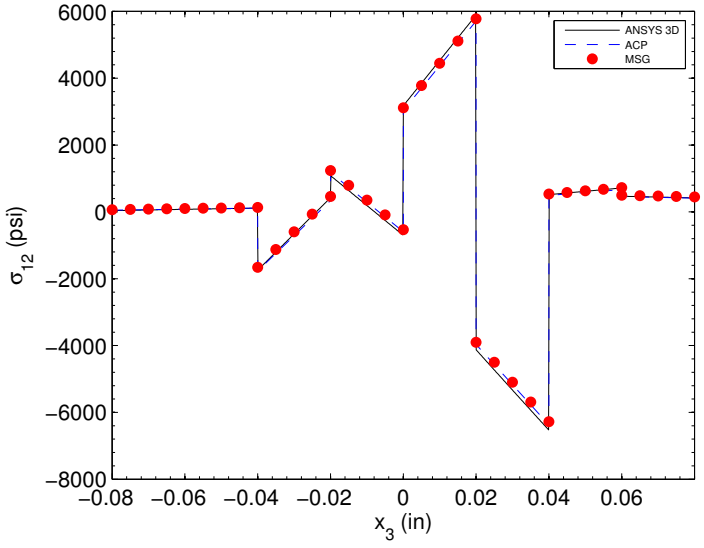

Figure 4.14. Comparison of stress σ_{12} through thickness for case 2

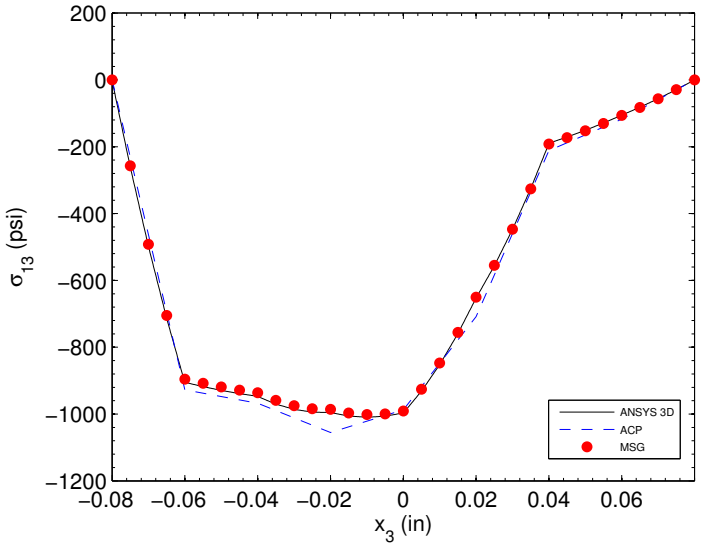

Figure 4.15. Comparison of stress σ_{13} through thickness for case 2

In terms of efficiency, the computation time among the three approaches are compared. It takes 4 hours, 58 minutes and 45 seconds to build and solve the model by ANSYS 3D with 16 CPUs. For MSG, it takes less than 1 minute to build and

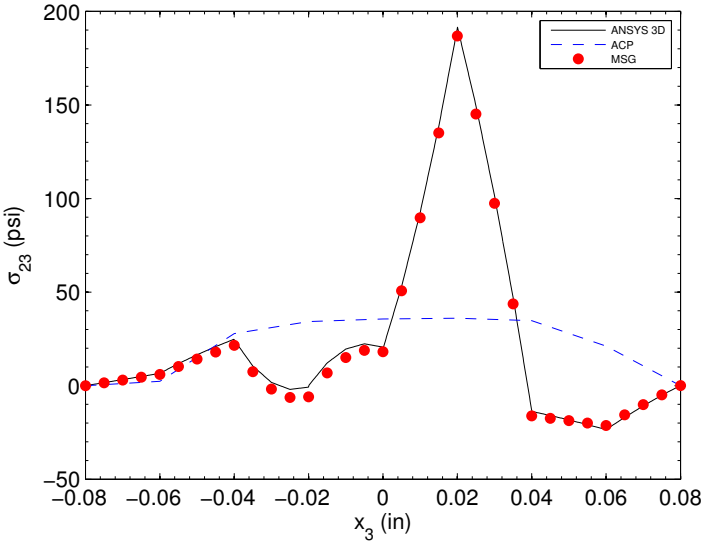

Figure 4.16. Comparison of stress σ_{23} through thickness for case 2

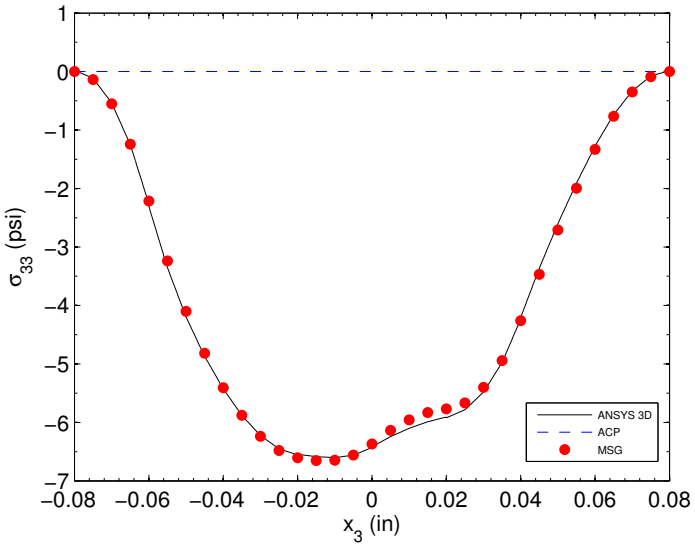

Figure 4.17. Comparison of stress σ_{33} through thickness for case 2

solve the model with 2 CPUs. The comparison of computation time for the three approaches is listed in Table 4.4.

Table 4.4 Computation time for case 2

Approach		**CPUs**	**Time**	
ANSYS 3D		16	4 h 58 min and 45 sec	
ACP		2	48 sec	
MSG	Homogenization	2	1 sec	32 sec
	Structural analysis	2	30 sec	
	Dehomogenization	2	1 sec	

It is clear that MSG is $4,481$ times more efficient than ANSYS 3D and is even slightly faster than ACP.

4.3 Case 3: A Kiteboard

The third case is a Kiteboard. This case is modified from the tutorial example of ANSYS Composite PrepPost Users Guide [18]. The bottom of the kiteboard are three plies arranged as a [-45/0/45] laminate. On top of those layers, there is a sandwich core. On top of the sandwich core, there is another [-45/0/45] laminate, which is the same as the bottom. For simplicity, each layer of the [-45/0/45] laminate is assumed to be orthotropic and has a thickness of 2 mm. The lamina constants of the [-45/0/45] laminate are $E_1 = 120$ GPa, $E_2 = E_3 = 86$ GPa, $G_{12} = G_{13} = 47$ GPa, $G_{23} = 31$ GPa, $\nu_{12} = \nu_{13} = 0.28$, $\nu_{23} = 0.4$. The sandwich core is assumed to be isotropic and has a thickness of 8 mm. The lamina constants of the sandwich core are $E = 6$ GPa, $\nu = 0.35$. The geometry and boundary conditions of the kiteboard are depicted in Figure 4.18. It is clamped at $x_1 = -700$ and subjected to point force $F_2 = 1000$ N at $(700, 0, 0)$. It is noted that this case is not exactly the same as the tutorial example from ANSYS. The thickness of [-45/0/45] is changed to be thicker so that the 3D model is easier to model. Also, the geometry and boundary conditions are simplified.

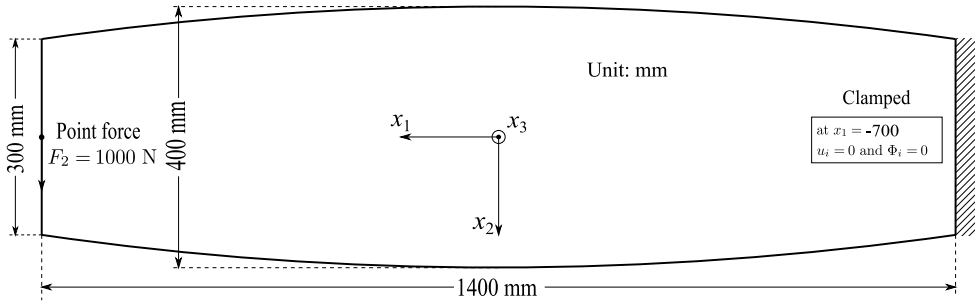

Figure 4.18. Geometry and boundary condition for case 3

The ANSYS 3D has 819,641 elements and 3,381,351 nodes as shown in Figure 4.19. There are 4 elements through the thickness of each layer of [-45/0/45] laminate and 32 elements through the thickness of the sandwich core. Both MSG and ACP

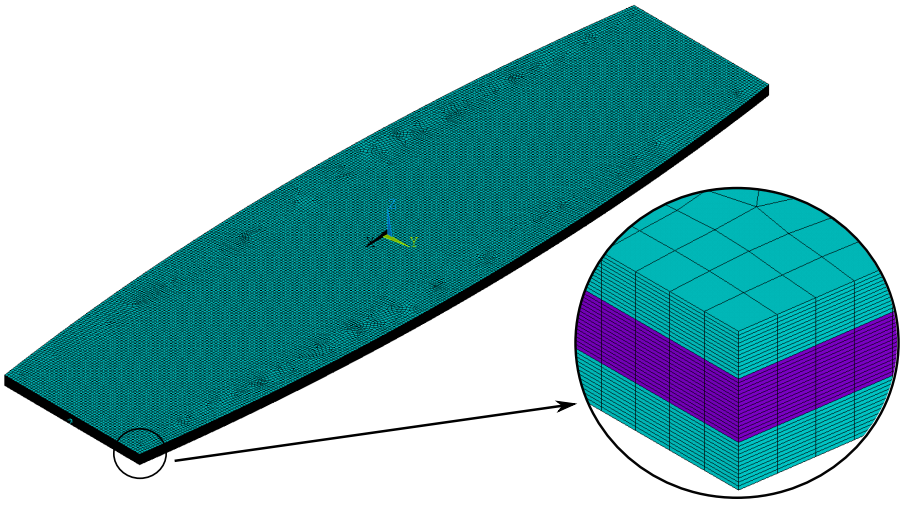

Figure 4.19. ANSYS 3D model for case 3

have $20,491$ elements and $62,150$ nodes for the 2D plate analysis. In addition, MSG uses 8 more line elements with 33 nodes for MSG homogenization and dehomogenization analysis. The total number of elements and nodes of the three approaches are summarized in Table 4.5.

Table 4.5 Finite element mesh information for case 3

Approach		**Element type**	**Elements**	**Nodes**
ANSYS 3D		SOLID186	$819,641$	$3,381,351$
ACP		SHELL281	$20,491$	$62,150$
MSG	SG	-	8	33
	2D Plate	SHELL281	$20,491$	$62,188$

The displacement u_3 by the three approaches is shown in Figure 4.20. The displacement values are taken along a path from point $(-700, 0, 0)$ to point $(700, 0, 0)$. As we can see, the displacement u_3 of both MSG and ACP agree well with ANSYS 3D.

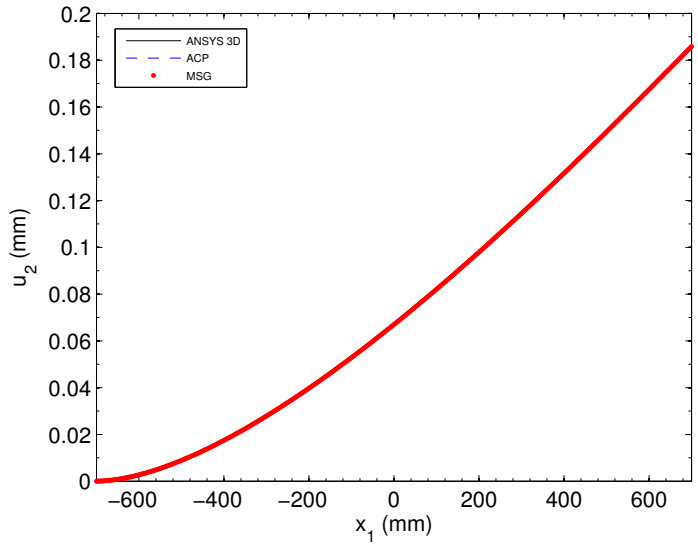

Figure 4.20. Comparison of deflection u_2 along x_1 at $x_2 = x_3 = 0$ for case 3

The stresses obtained from the three approaches are compared. The stress values are taken through thickness at the center node ($x_1 = 0,\ x_2 = 0$). For ANSYS 3D, it is taken along a path from point $(0, 0, -10)$ to point $(0, 0, 10)$.

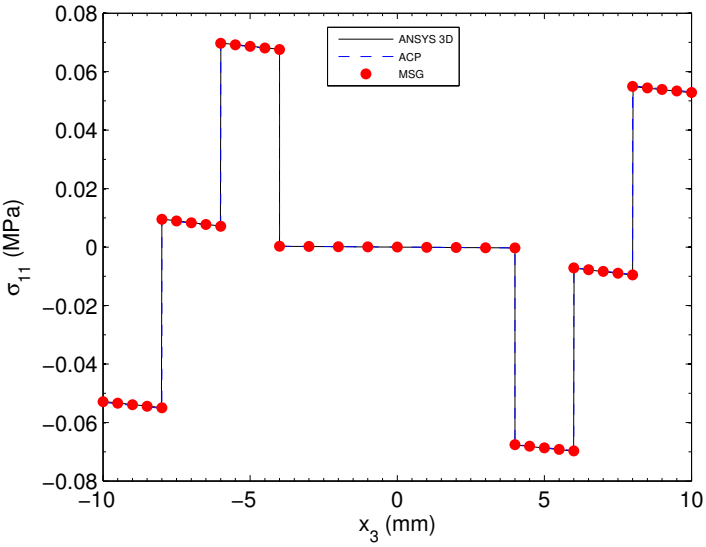

Figure 4.21. Comparison of stress σ_{11} through thickness for case 3

For in-plane stresses, both MSG and ACP agree well with ANSYS 3D as shown from Figure 4.21 to Figure 4.23.

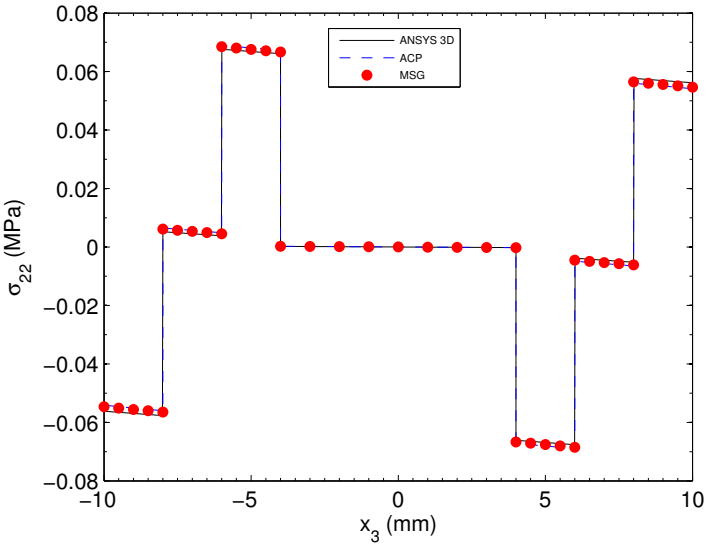

Figure 4.22. Comparison of stress σ_{22} through thickness for case 3

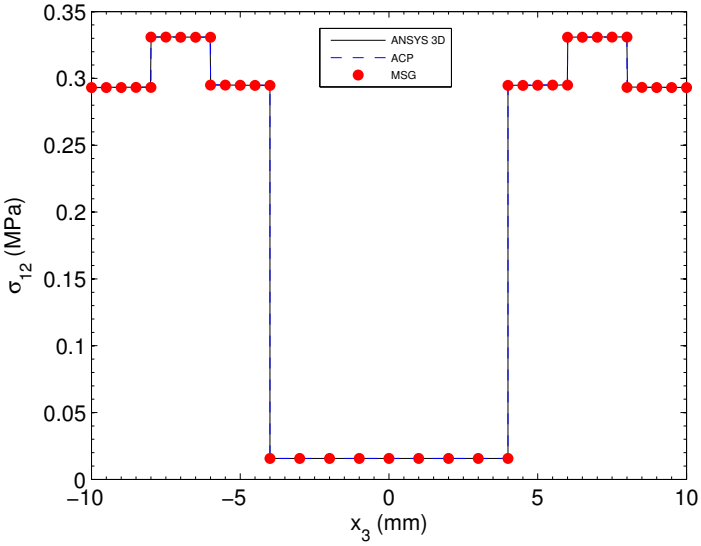

Figure 4.23. Comparison of stress σ_{12} through thickness for case 3

For transverse stresses, MSG agrees well with ANSYS 3D while ACP loses accuracy as shown from Figure 4.24 to Figure 4.26. For σ_{13}, ACP can not capture the variation of stress. For σ_{23} and σ_{33}, ACP only gives a constant zero value.

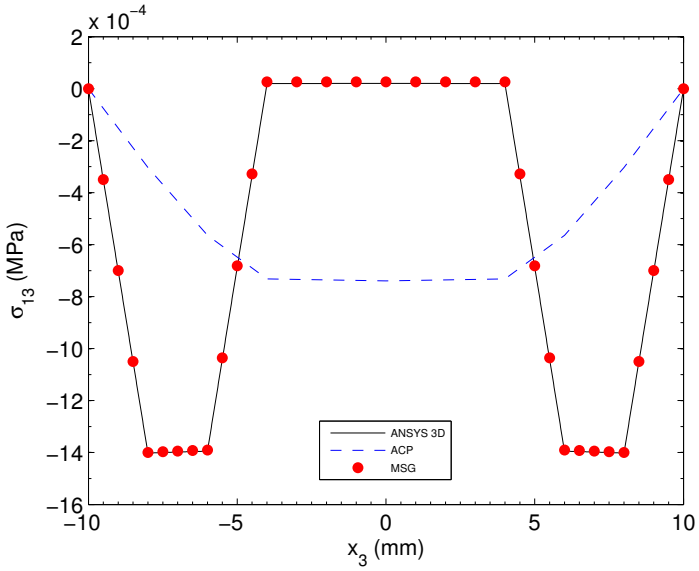

Figure 4.24. Comparison of stress σ_{13} through thickness for case 3

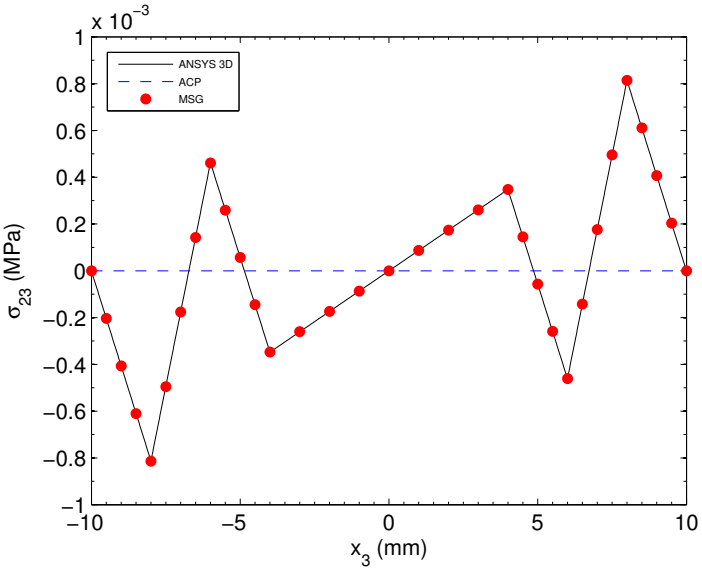

Figure 4.25. Comparison of stress σ_{23} through thickness for case 3

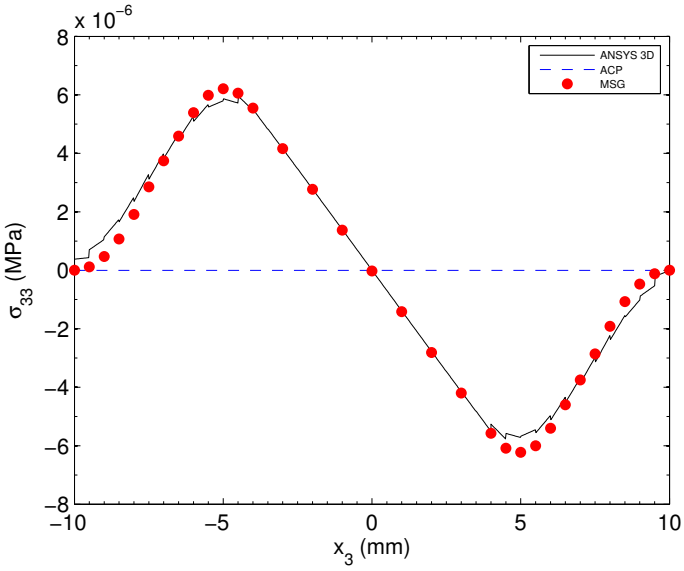

Figure 4.26. Comparison of stress σ_{33} through thickness for case 3

In terms of efficiency, the computation time among the three approaches are compared. It takes 5 hours, 2 minutes and 58 seconds to build and solve the model by ANSYS 3D with 16 CPUs. For MSG, it takes less than 1 minute to build and solve the model with 2 CPUs. The comparison of computation time for the three approaches is listed in Table 4.6.

Table 4.6 Computation time for case 3

Approach		**CPUs**	**Time**	
ANSYS 3D		16	5 h 2 min 58 sec	
ACP		2	56 sec	
MSG	Homogenization	2	1 sec	36 sec
	Structural analysis	2	34 sec	
	Dehomogenization	2	1 sec	

It is clear that MSG is $4,039$ times more efficient than ANSYS 3D and is even slightly faster than ACP.

4.4 Case 4: A Roof Sandwich Panel

The forth case is a roof sandwich panel, which is widely used in the construction of house roof as shown in Figure 4.27. It is a composite plate made of three layers: low density sandwich core inserted between two relatively thin skin layers. For simplicity, both the sandwich core and the skin layers are assumed to be isotropic. The material properties of the sandwich core is $E = 600$ MPa, $\nu = 0.35$. The material properties of the skin layers are $E = 68.9$ GPa, $\nu = 0.33$. The cross section geometry of the roof sandwich panel is depicted in Figure 4.28, which is repeated five times in x_2 direction for the whole structure. The whole structure is a 1000 mm $\times$ 1000 mm plate, which is clamped at $x_1 = -500$ and subjected to point force $F_1 = 10$ kN at $(500, 0, 0)$. Since this structure features 2D heterogeneity, the corresponding SG will be 2D as depicted in Figure 4.29.

Figure 4.27. Application of roof sandwich panels

The ANSYS 3D has $871,201$ elements and $3,715,696$ nodes as shown in Figure 4.30. Both MSG and ACP have $14,401$ elements and $43,682$ nodes for the 2D plate analysis. In addition, MSG uses $1,452$ more elements with $4,623$ nodes for MSG

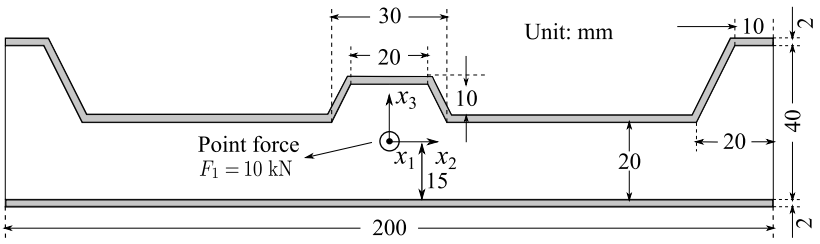

Figure 4.28. Geometry and boundary condition for case 4

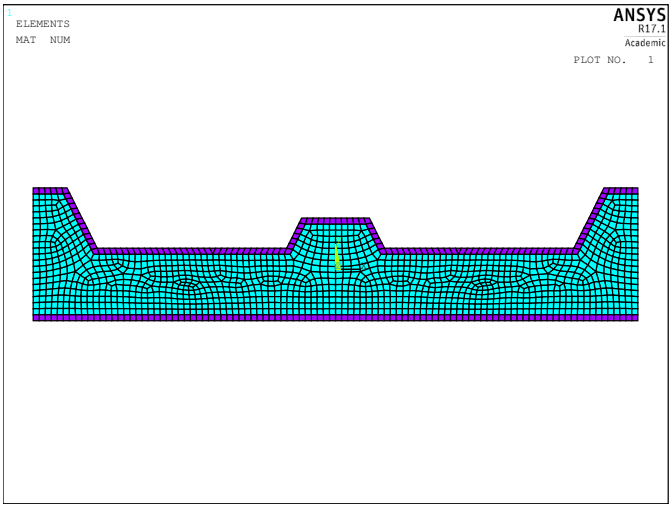

Figure 4.29. 2D SG for roof sandwich panel

homogenization and dehomogenization analysis. The total number of elements and nodes of the three approaches are summarized in Table 4.9.

For ACP, the model is made of three layers. The thickness of the sandwich core is 20 mm and the thickness of the skin layers is the same as ANSYS 3D.

The displacement u_1 and u_3 by the three approaches are shown in Figure 4.31 and Figure 4.32. The displacement values are taken along a path from point $(-500, 0, 0)$ to point $(500, 0, 0)$. As we can see, MSG agrees well with ANSYS 3D for both u_1 and u_3. For u_1, ACP loses significant accuracy when approaching to $x_1 = 500$. For u_3,

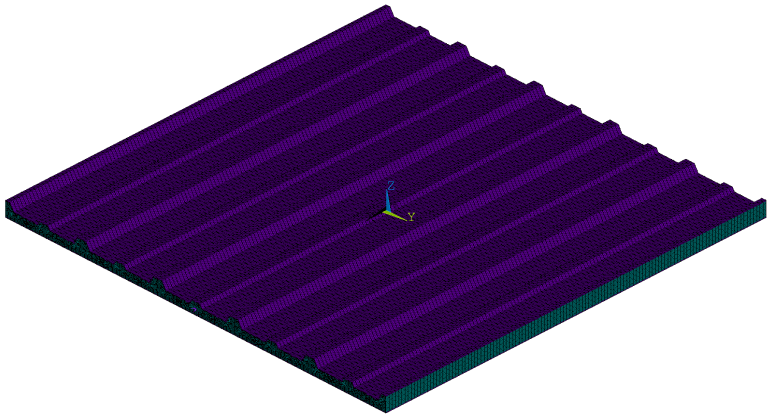

Figure 4.30. ANSYS 3D model case 4

Table 4.7 Finite element mesh information for case 4

Approach		**Element type**	**Elements**	**Nodes**
ANSYS 3D		SOLID186	871,201	3,751,696
ACP		SHELL281	14,401	43,682
MSG	SG	-	1,452	4,623
	2D Plate	SHELL281	14,401	43,682

ACP only gives a constant zero value. Because the point force is applied at the middle of the thickness, there is no coupling between force and moment in ACP. However, the coupling exists in 3D model due to the variation of thickness.

The stresses obtained from the three approaches are compared. The stress values are taken at $x_1 = 0,\ x_2 = 0$ through thickness. Since the shear stress components σ_{12}, σ_{13} and σ_{23} are in the magnitude of 0.1 Pa or less, these stress components are not compared. For ANSYS 3D, it is taken along a path from point $(0, 0, -10)$ to point $(0, 0, 10)$.

For σ_{11}, σ_{22} and σ_{33}, MSG agrees well with ANSYS 3D as shown in 4.33 to Figure 4.35 while ACP loses accuracy. For σ_{11} and σ_{22}, the loss of accuracy is obvious at the

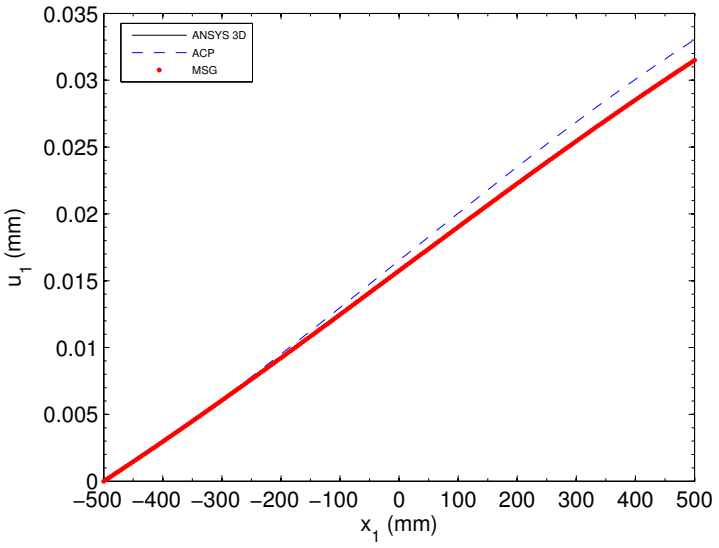

Figure 4.31. Comparison of deflection u_2 along $x_2 = 0$ for case 4

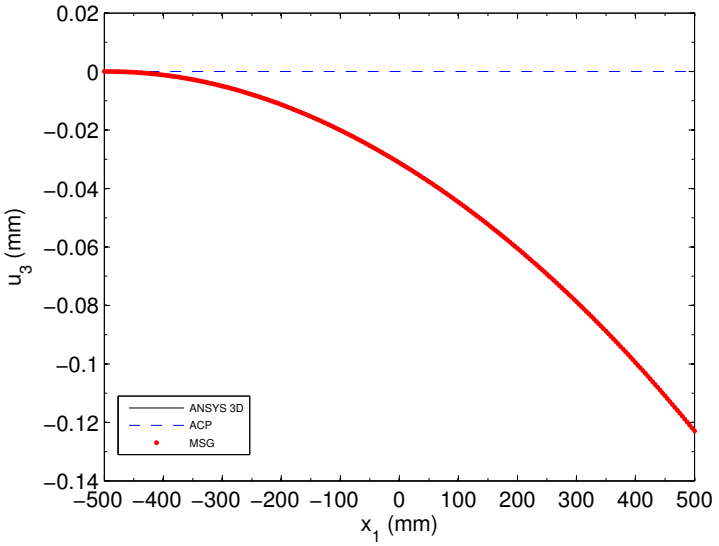

Figure 4.32. Comparison of deflection u_2 along $x_2 = 0$ for case 4

skin layers. For σ_{33}, ACP only gives a constant zero value since there is no applied pressure.

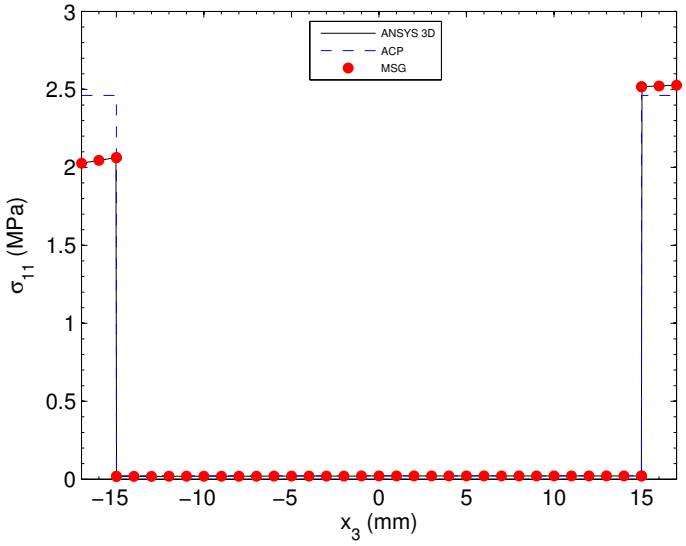

Figure 4.33. Comparison of stress σ_{11} through thickness for case 4

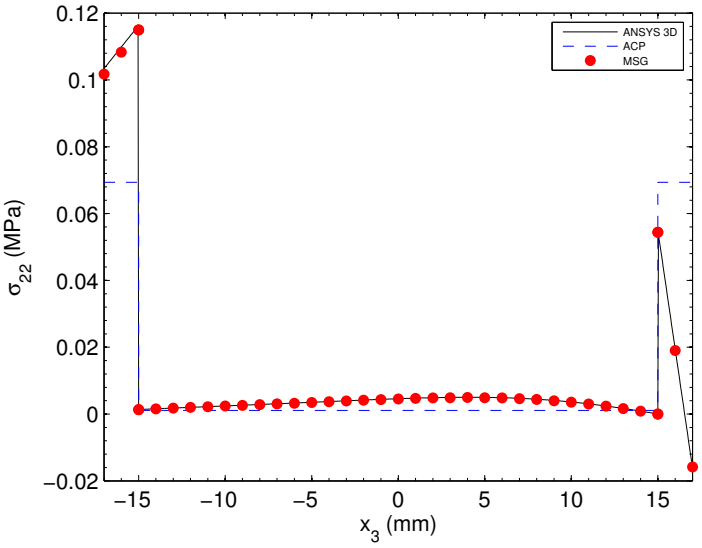

Figure 4.34. Comparison of stress σ_{22} through thickness for case 4

In terms of efficiency, the computation time among the three approaches are compared. It takes 6 hours, 21 minutes and 45 seconds to build and solve the model by ANSYS 3D with 16 CPUs. For MSG, it takes less than 1 minute to build and

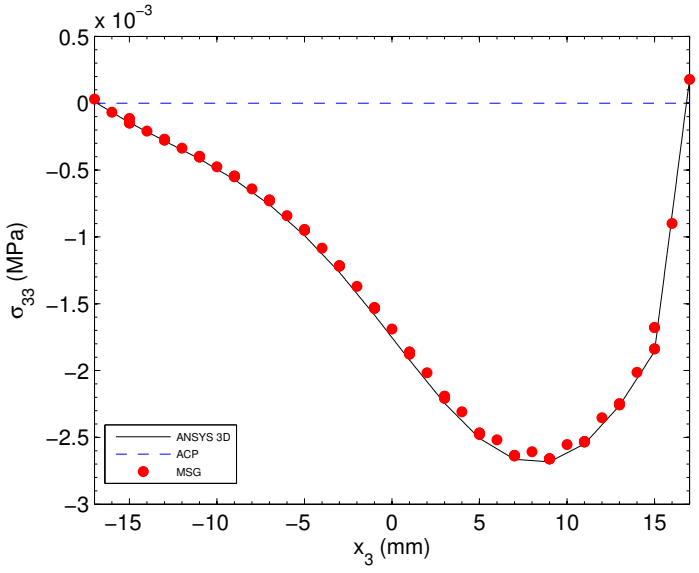

Figure 4.35. Comparison of stress σ_{33} through thickness for case 4

solve the model with 2 CPUs. The comparison of computation time for the three approaches is listed in Table 4.8.

Table 4.8 Computation time for case 4

Approach		**CPUs**	**Time**	
ANSYS 3D		16	6 h 21 min 45 sec	
ACP		2	28 sec	
MSG	Homogenization	2	5 sec	44 sec
	Structural analysis	2	23 sec	
	Dehomogenization	2	16 sec	

It is clear that MSG is $4,164$ times more efficient than ANSYS 3D.

4.5 Case 5: A Corrugated-core Sandwich Panel

The fifth case is a corrugated-core sandwich panel, which is also widely used in industry because of its high bending stiffness to weight ratio. A sample aluminum corrugated sandwich panel is illustrated in Figure 4.36. The thin skin layers are high in stiffness when compared to the corrugated core. For simplicity, both the corrugated core and skin layers are assumed to be isotropic. The material properties [27] of the corrugated core is $E = 4.5$ GPa, $\nu = 0.225$. The material properties of the skin layers are $E = 68.9$ GPa, $\nu = 0.33$. The cross section geometry of the corrugated-core sandwich panel is depicted in Figure 4.37, which is repeated seven times in x_2 direction for the whole structure. The whole structure is a 200 mm $\times$ 203.7 mm plate, which is clamped at $x_1 = -100$ and subjected to point force $F_1 = 10$ kN and $F_2 = 10$ kN at $(100, 0, 0)$. Since this structure features 2D heterogeneity, the corresponding SG will be 2D as depicted in Figure 4.38.

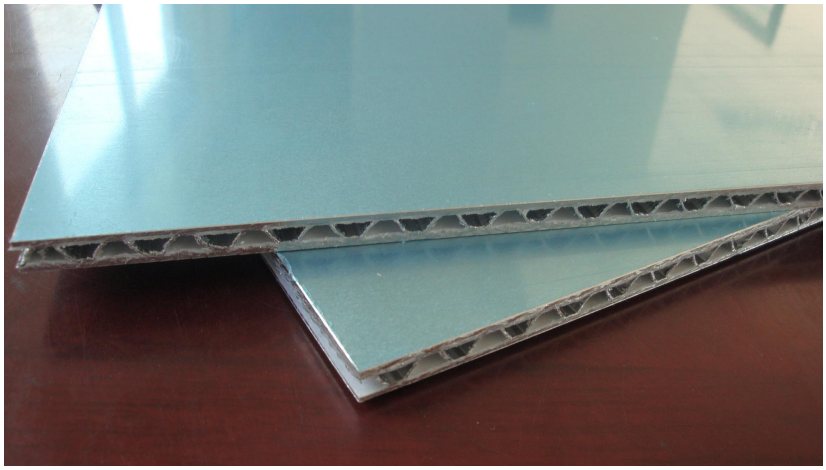

Figure 4.36. Aluminum Corrugated Sandwich Panel

The ANSYS 3D has $1,422,401$ elements and $6,958,887$ nodes as shown in Figure 4.39. Both MSG and ACP have $25,601$ elements and $77,442$ nodes for the 2D plate analysis. In addition, MSG uses $1,016$ more elements with $3,658$ nodes for MSG

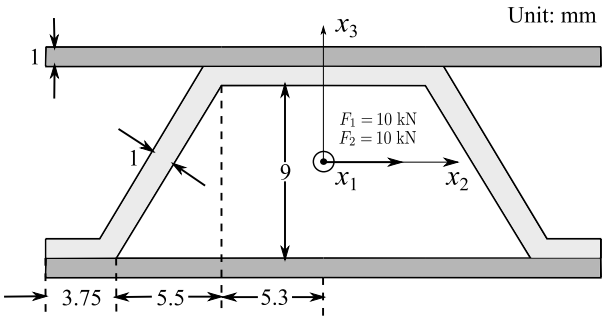

Figure 4.37. Geometry and boundary condition for case 5

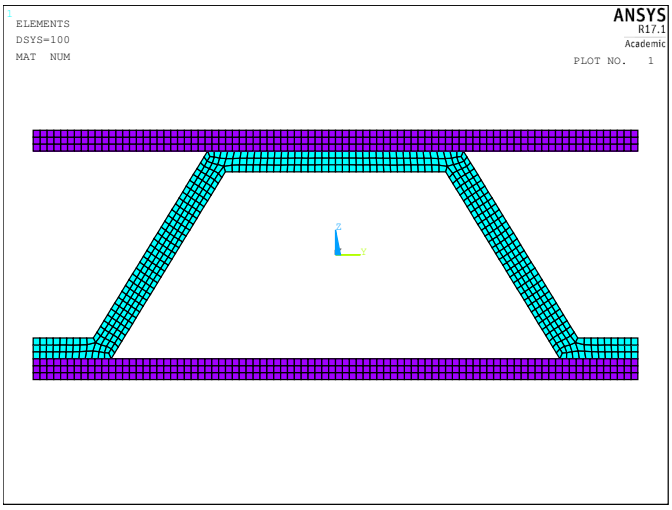

Figure 4.38. 2D SG for corrugated-core sandwich panel

homogenization and dehomogenization analysis. The elements number and nodes number of the three approaches are summarized in Table 4.9.

For ACP, the model is made of three layers. The material properties of the corrugated core is the smeared material properties of the original core since there are void. The Poisson's ratio remains the same while the Young's modulus of the smeared corrugated core becomes

$$E^* = E\frac{A_c}{A} = 4.5 \times 10^3 \times \frac{44.46}{291} = 687.53 \text{ MPa} \tag{4.1}$$

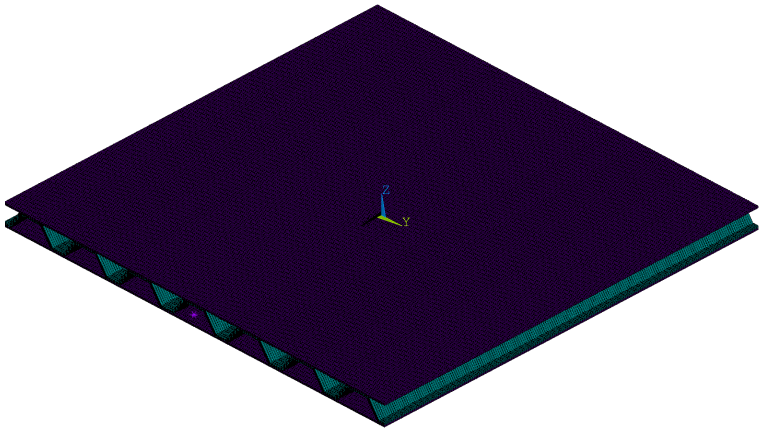

Figure 4.39. The magnitude of displacement by ANSYS 3D for case 5

Table 4.9 Finite element mesh information for case 5

Approach		**Element type**	**Elements**	**Nodes**
ANSYS 3D		SOLID186	$1,442,401$	$6,958,887$
ACP		SHELL281	$25,601$	$77,442$
MSG	SG	-	$1,016$	$3,658$
	2D Plate	SHELL281	$25,601$	$77,442$

where A_c is the area of sandwich the core and A is the area between the the skin layers (not include the skins) in Figure 4.37.

The displacement u_1 and u_2 are compared at point $(0, 4, 0)$ as shown in Table 4.10. For u_1, both ACP and MSG have difference less than 1% to ANSYS 3D. For u_2, MSG has difference less than 1% to ANSYS 3D while ACP has difference 1.176% to ANSYS 3D.

The stresses obtained from the three approaches are compared. The stress values are taken through the thickness along $(0, 0, 4)$ to $(0, 0, 6)$. Since the transverse stress components σ_{13}, σ_{23} and σ_{33} are in the magnitude of 0.1 Pa or less, these stress components are not compared.

Table 4.10 Comparison of u_1 and u_2 at point $(0, 4, 0)$ for case 5

Approach	u_1 (mm)	u_2 (mm)
ANSYS 3D	3.281364E-02	1.798312E-01
ACP	3.290286E-02	1.777169E-01
MSG	3.292460E-02	1.800830E-01

For σ_{11}, σ_{22} and σ_{12}, MSG agrees well with ANSYS 3D as shown in Figure 4.40 to Figure 4.42 while ACP loses accuracy. The loss of accuracy is obvious at the corrugated core for σ_{11} and σ_{12}. And the loss of accuracy is obvious at the skin layer for σ_{22}.

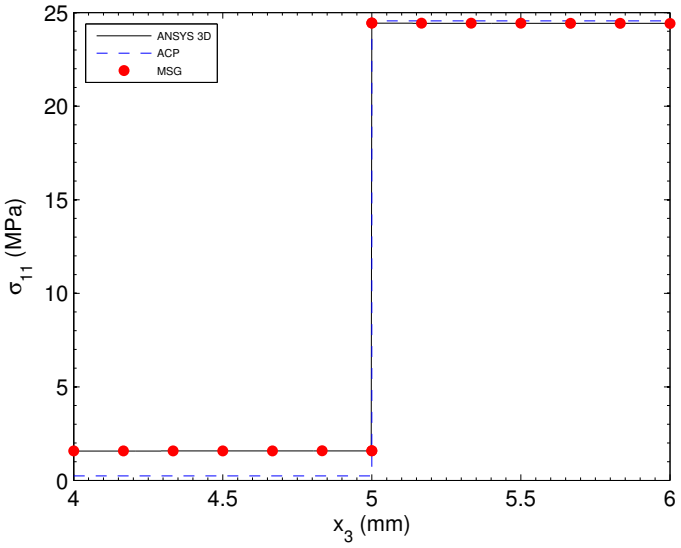

Figure 4.40. Comparison of stress σ_{11} through thickness for case 5

In terms of efficiency, the computation time among the three approaches are compared. It takes 5 hours, 20 minutes and 30 seconds to build and solve the model by ANSYS 3D with 16 CPUs. For MSG, it takes less than 1 minute to build and

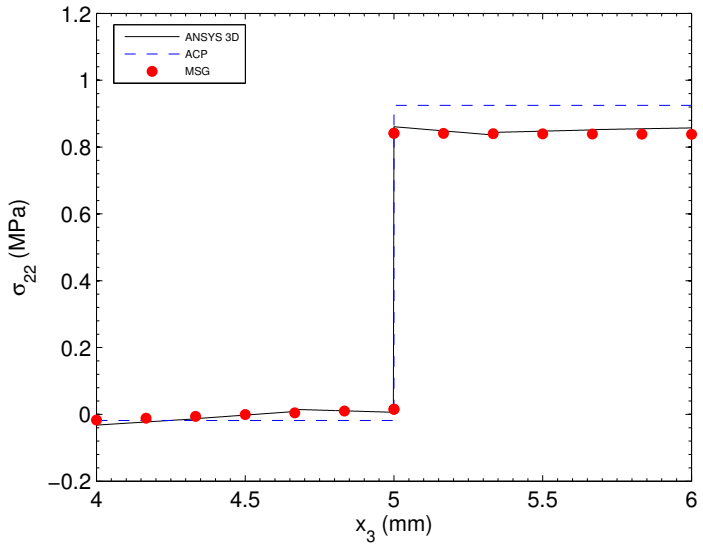

Figure 4.41. Comparison of stress σ_{22} through thickness for case 5

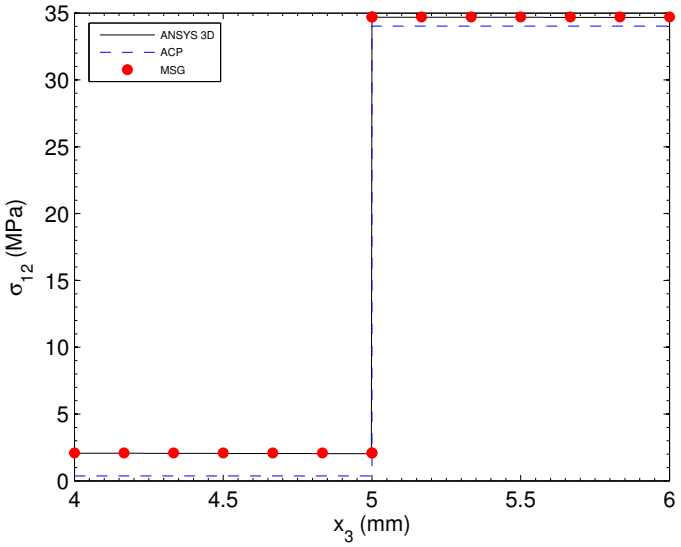

Figure 4.42. Comparison of stress σ_{12} through thickness for case 5

solve the model with 2 CPUs. The comparison of computation time for the three approaches is listed in Table 4.11.

Table 4.11 Computation time for case 5

Approach		**CPUs**	**Time**	
ANSYS 3D		16	5 h 20 min 30 sec	
ACP		2	41 sec	
MSG	Homogenization	2	3 sec	42 sec
	Structural analysis	2	31 sec	
	Dehomogenization	2	8 sec	

It is clear that MSG is $3,662$ times more efficient than ANSYS 3D and as fast as ACP.

5. SUMMARY

In this thesis, Mechanics of Structure Genome (MSG) has been used to analyze composite plates. A simple graphic user interface (GUI) named ANSYS-SwiftComp GUI has been developed based on ANSYS platform as a user friendly GUI to improve the user friendliness of MSG. The numerical cases show that the MSG approach is not only accurate but also efficient in comparison to the ANSYS 3D approach and the ACP approach. The following accomplishments are achieved during this study:

1. ANSYS-SwiftComp GUI has been developed, which can use the preprocessing and postprocessing capability of ANSYS as a user friendly GUI for SwiftComp$^{\text{TM}}$. ANSYS-SwiftComp GUI can easily create 1D, 2D or 3D SGs and generate the corresponding input files for SwiftComp$^{\text{TM}}$ homogenization and dehomogenization, which greatly enhances the convenience to use SwiftComp$^{\text{TM}}$.

2. The steps of modeling composite plates by using the MSG approach are demonstrated by five numerical cases. When compared with the ANSYS 3D approach, the MSG approach agrees well with the results, which reveals its accuracy. When compared with the ACP approach, the MSG approach presents the same computational efficiency while being more accurate.

3. The first-order shear deformation theory (FSDT) is derived and compared in detail with the Reissner-Mindlin plate model based on VAM. The limitations of FSDT are discussed while the advantages of plate model using VAM are presented.

Although the power of MSG to analyze composite plates has been shown and the GUI based on ANSYS has been developed, there are still some work to be continued and investigated in the future.

1. ANSYS SHELL281 or SHELL181 elements can read A, B, D and G matrix and output global behavior element-wise. However, new shell element is needed to read the coupling terms Y matrix if one uses Reissner-Mindlin plate model in SwiftComp$^{\text{TM}}$. Also the new shell element should output global behavior point-wise at each Gaussian point, which will be more accurate. And the derivatives of 2D strain measures should also be represented at each Gaussian point if one uses the Reissner-Mindlin plate model.

2. Present work only used 1D and 2D SGs for composite plates. In some cases such as honeycomb sandwich structure, only 3D SG can capture the heterogeneity of the original structure. So some numerical cases by using 3D SGs are needed to further reveal the capability of MSG.

LIST OF REFERENCES

LIST OF REFERENCES

[1] *ANSYS Mechanical APDL Element Reference*, January 2016. Release 17.0.

[2] R. D. Mindlin. Influence of rotary inertia and shear on flexural motions of isotropic elastic plates. *ASME Journal of Applied Mechanics*, 18:31–38, 1951.

[3] E. Reissner. The effect of transverse shear deformation on the bending of elastic plates. *ASME Journal of Applied Mechanics*, 12:A68–A77, 1945.

[4] R. Khandan, S. Noroozi, P. Sewell, and J. Vinney. The development of laminated composite plate theories: a review. *Journal of Materials Science*, 47(16):5901–5910, 2012.

[5] J. N. Reddy. A simple higher-order theory for laminated composite plates. *Journal of Applied Mechanics*, 51(4):745–752, 1984.

[6] V. L. Berdichevskii. Variational-asymptotic method of constructing a theory of shells: PMM vol. 43, no.4, 1979, pp. 664687. *Journal of Applied Mathematics and Mechanics*, 43:711–736, 1979.

[7] A. R. Atilgan and D. H. Hodges. On the strain energy of laminated composite plates. *International Journal of Solids and Structures*, 29(20):2527–2543, 1992.

[8] V. G. Sutyrin and D. H. Hodges. On asymptotically correct linear laminated plate theory. *International Journal of Solids and Structures*, 33(25):3649–3671, 1996.

[9] W. Yu, D. H. Hodges, and V. V. Volovoi. Asymptotic construction of reissner-like composite plate theory with accurate strain recovery. *International Journal of Solids and Structures*, 39(20):5185–5203, 2002.

[10] W. Yu. *Variational asymptotic modeling of composite dimensionally reducible structures*. PhD thesis, Georgia Institute of Technology, 2002.

[11] W. Yu, D. H. Hodges, and V. V. Volovoi. Asymptotic generalization of reissner–mindlin theory: accurate three-dimensional recovery for composite shells. *Computer Methods in Applied Mechanics and Engineering*, 191(44):5087–5109, 2002.

[12] W. Yu, D. H. Hodges, and V. V. Volovoi. Asymptotically accurate 3-d recovery from reissner-like composite plate finite elements. *Computers & Structures*, 81(7):439–454, 2003.

[13] W. Yu. A unified theory for constitutive modeling of composites. *Journal of Mechanics of Materials and Structures*, 11(4):379–411, 2016.

[14] C. E. S. Cesnik and D. H. Hodges. Vabs: a new concept for composite rotor blade cross-sectional modeling. *Journal of the American Helicopter Society*, 42(1):27–38, 1997.

[15] W. Yu and T. Tang. Variational asymptotic method for unit cell homogenization of periodically heterogeneous materials. *International Journal of Solids and Structures*, 44(11):3738–3755, 2007.

[16] X. Liu and W. Yu. A novel approach to analyze beam-like composite structures using mechanics of structure genome. *Advances in Engineering Software*, 100:238–251, 2016.

[17] B. Peng, J. Goodsell, R. B. Pipes, and W. Yu. Generalized free-edge stress analysis using mechanics of structure genome. *Journal of Applied Mechanics*, 83(10):101013, 2016.

[18] *ANSYS Composite PrepPost User's Guide*, January 2016. Release 17.0.

[19] B. Zhao, F. Jiang, Z. Ye, and W. Yu. *ANSYS-SwiftComp GUI 1.0 User's Manual*. West Lafayette, IN 47907, May 2016.

[20] W. Yu. Journal Club Theme of October 2015: Mechanics of Structure Genome. http://imechanica.org/node/18928.

[21] W. Yu. *SwiftComp User Manual*. West Lafayette, IN 47907, July 2016.

[22] C. T. Sun and R. S. Vaidya. Prediction of composite properties from a representative volume element. *Composites Science and Technology*, 56(2):171–179, 1996.

[23] W. Yu. Classical Plate Model. http://imechanica.org/files/plate.pdf, April 2012.

[24] Y. Long. Asymptotic modelling of a thermopiezoelastic anisotropic smart plate. Master's thesis, Purdue University, 2015.

[25] *ANSYS Mechanical APDL Theory Reference*, August 2016. Release 17.2.

[26] *ABAQUS Theory Manual Version 6.8*, 2008.

[27] I. Dayyani, S. Ziaei-Rad, and M. I. Friswell. The mechanical behavior of composite corrugated core coated with elastomer for morphing skins. *Journal of Composite Materials*, 48(13):1623–1636, 2014.

[28] F. Jiang and W. Yu. *ANSYS-VABS Graphic User Interface (GUI) Release Alpha-1.0 (in updating)*. West Lafayette, IN 47907, Aug 2015.

APPENDICES

A. CALCULATION OF SHEAR CORRECTION FACTORS

Consider a composite plate as shown in Figure 3.1. Assume only bending and shear in the x_1 direction, without gradients in the x_2 direction. Then the in-plane forces in the composite plate are zero $N_{11} = N_{22} = N_{12} = 0$ and $\frac{\partial}{\partial x_2} = 0$ for all response variables. Then the equilibrium equation in the x_1 direction is

$$\sigma_{11,1} + \sigma_{13,3} = 0 \tag{A.1}$$

The 2D equilibrium equations from Eq. (3.27) become

$$M_{11,1} - N_{13} = 0 \tag{A.2}$$

From Eq. (3.19), we have

$$\begin{Bmatrix} \epsilon \\ \kappa \end{Bmatrix} = H \begin{Bmatrix} N \\ M \end{Bmatrix} \tag{A.3}$$

where

$$H = \begin{bmatrix} A & B \\ B & D \end{bmatrix}^{-1}$$

We also assume $M_{22} = M_{12} = 0$. Thus,

$$\begin{Bmatrix} \epsilon \\ \kappa \end{Bmatrix} = \begin{bmatrix} H_{14} & H_{24} & H_{34} & H_{44} & H_{54} & H_{64} \end{bmatrix}^{\mathrm{T}} M_{11} \tag{A.4}$$

where H_{i4} is the fourth column of H. Substituting Eq. (A.4) into Eq. (3.6) and then into Eq. (3.8), we get in-plane stress components in terms of M_{11} as

$$\sigma_{11} = (P_1 + x_3 P_2) M_{11} \tag{A.5}$$

where

$$P_1 = Q_{11} H_{14} + Q_{12} H_{24} + Q_{16} H_{34}$$

and

$$P_2 = Q_{11}H_{44} + Q_{12}H_{54} + Q_{16}H_{64}$$

Combining the gradient of this equation with the equilibrium equations in Eq. (A.1) and Eq. (A.2), we get

$$\sigma_{13,3} = -(P_1 + x_3 P_2)N_{13} \tag{A.6}$$

A composite plate consists of N layers $1, 2, 3, ...$ with different values of (P_1^1, P_2^1) at layer 1, (P_1^2, P_2^2) at layer 2, ... (P_1^N, P_2^N) at layer N. Layer i extends from z_i to z_{i+1} and its thickness is $t_i = z_{i+1} - z_i$. Integrating Eq. (A.6) through the plate and using the boundary conditions $\sigma_{13} = 0$ at $x_3 = 0$, $\sigma_{13}^i = \sigma_{13}^{i+1}$ at $x_3 = z_{i+1}$ and $\sigma_{13} = 0$ at $x_3 = z_{N+1}$, gives the transverse shear stress in layer i as

$$\sigma_{13}^i = -\big[P_1^i(x_3 - z_i) + \frac{1}{2}(x_3^2 - z_i^2)P_2^i + P_3^i\big]N_{13} \tag{A.7}$$

where

$$P_3^i = \sum_{j=1}^{i-1} t_j \big[P_1^j + \frac{1}{2}(z_{i+1} + z_i)P_2^j\big] \tag{A.8}$$

We can find σ_{23} through the thickness of a composite plate using a similar procedure by assuming only bending and shear in the x_2 direction

$$\sigma_{23}^i = -\big[P_4^i(x_3 - z_i) + \frac{1}{2}(x_3^2 - z_i^2)P_5^i + P_6^i\big]N_{23} \tag{A.9}$$

where

$$P_6^i = \sum_{j=1}^{i-1} t_j \big[P_4^j + \frac{1}{2}(z_{i+1} + z_i)P_5^j\big] \tag{A.10}$$

Equating the strain energy due to transverse shear stress resultant with the strain energy due to the true transverse shear stresses obtained above

$$\frac{1}{2}\begin{bmatrix} N_{13} & N_{23} \end{bmatrix} S_s^s \begin{Bmatrix} N_{13} \\ N_{23} \end{Bmatrix} = \frac{1}{2}\sum_{i=1}^{N} \int_{z_i}^{z_{i+1}} \begin{bmatrix} \sigma_{13}^i & \sigma_{23}^i \end{bmatrix} S_s^i \begin{Bmatrix} \sigma_{13}^i \\ \sigma_{23}^i \end{Bmatrix} dx_3 \tag{A.11}$$

where S_s^s is the transverse shear compliance matrix of the section and S_s^i is the transverse shear compliance matrix of layer i.

Substituting the relations for σ^i_{13} and σ^i_{23} into the above equation and solving for S^s_s, we get

$$\begin{aligned} S^s_{s\,11} = \sum_{i=1}^{N} S^i_{s11} t_i \big[(P^i_3)^2 + t_i P^i_3 (P^i_1 + z_i P^i_2) + \frac{1}{3} t_i^2 (P^i_1 + z_i P^i_2)^2 \\ - \frac{1}{4} t_i^3 P^i_2 (P^i_1 + z_i P^i_2)^2 + \frac{1}{20} t_i^4 (P^i_2)^2 \big] \end{aligned} \tag{A.12}$$

$$\begin{aligned} S^s_{s\,22} = \sum_{i=1}^{N} S^i_{s22} t_i \big[(P^i_6)^2 + t_i P^i_6 (P^i_4 + z_i P^i_5) + \frac{1}{3} t_i^2 (P^i_4 + z_i P^i_5)^2 \\ - \frac{1}{4} t_i^3 P^i_5 (P^i_4 + z_i P^i_5)^2 + \frac{1}{20} t_i^4 (P^i_5)^2 \big] \end{aligned} \tag{A.13}$$

$$\begin{aligned} S^s_{s\,12} = \sum_{i=1}^{N} S^i_{s12} t_i \Big[P^i_3 P^i_6 + \frac{1}{2} t_i \big[P^i_3 (P^i_4 + z_i P^i_5) + P^i_6 (P^i_1 + z_i P^i_2) \big] \\ + \frac{1}{3} t_i^2 (P^i_1 + z_i P^i_2)(P^i_4 + z_i P^i_5) \\ - \frac{1}{8} t_i^3 \big[P_2 (P^i_4 + z_i P^i_5) + P_5 (P^i_1 + z_i P^i_2) \big] \\ + \frac{1}{20} t_i^4 P^i_2 P^i_5 \Big] \end{aligned} \tag{A.14}$$

Then transverse shear stiffness matrix G is the inverse of S^s_s

$$G = \begin{bmatrix} S^s_{s\,11} & S^s_{s\,12} \\ S^s_{s\,12} & S^s_{s\,22} \end{bmatrix}^{-1} \tag{A.15}$$

The shear correction factors are $K = G\langle Q^* \rangle^{-1}$

B. ANSYS-SWIFTCOMP GUI

To facilitate the use of SwiftComp^{TM}, a simple graphic user interface (GUI) based on ANSYS, called ANSYS-SwiftComp GUI [19] is developed, which can be downloaded from cdmHUB: https://cdmhub.org/resources/1136 . The development of this GUI uses two languages, i.e., ANSYS Parametric Design Language (APDL) and User Interface Design Language (UIDL). The ANSYS-SwiftComp GUI is modified from the ANSYS-VAMUCH GUI developed by Zheng Ye and part of the macros are also inherited from ANSYS-VABS GUI [28] developed by Fang Jiang. Both ANSYS-VAMUCH GUI and ANSYS-VABS GUI are superseded by ANSYS-SwiftComp GUI.

B.1 ANSYS-SwiftComp GUI Overview

ANSYS-SwiftComp GUI is a graphic user interface integrated in the Main Menu of ANSYS, which can use the preprocessing and postprocessing capability of ANSYS as a user friendly GUI for SwiftComp^{TM}. The newly added functions specific for SwiftComp^{TM} are located in the Preprocessor menu and the Solution menu in ANSYS as shown in Figure B.1. The functions including Common SGs, Homogenization and Dehomogenization are completely new to ANSYS and will be explained in the following:

The first level menu of ANSYS-SwiftComp GUI composes of three major menus: Preprocessor, Solution and General Postproc.

Preprocessor menu

Material Props: Users can define isotropic, orthotropic or general anisotropic material properties under this menu by using Material Models function.

Modeling: Users can build their own models by elementary entities which contain all basic geometry elements (e.g. point, line, surface, and volume).

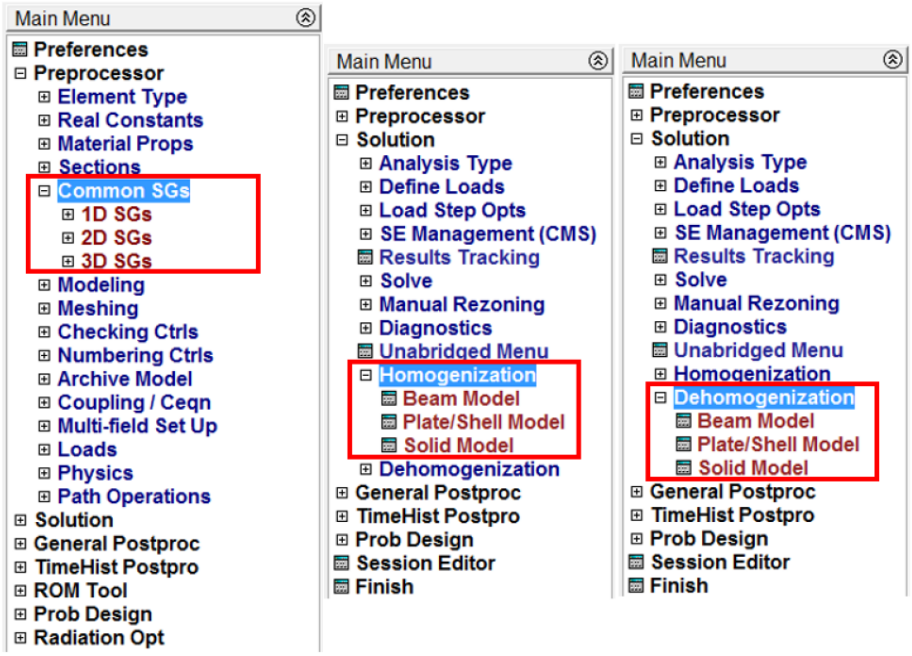

Figure B.1. Customized menu structure of ANSYS-SwiftComp GUI

Common SGs: Users can create their model through Common SGs, which provides several common fundamental building blocks of composite materials and structures.

Mesh: Generate mesh according to the geometry of model, and user can choose different mesh algorithms to meet their needs.

Solution menu

Homogenization: Users can invoke SwiftComp^{TM} to compute the effect properties for different structural models (beams, plates/shells or 3D structures).

Dehomogenization: After providing the global behavior, users can invoke SwiftComp^{TM} to compute the local fields including displacements, stresses and strains, and contour plots will be automatically generated after calculation is completed.

General Postproc menu

Plot Results: After Dehomogenization, users can choose different contour plots (displacements, stresses and strains) in this menu to visualize the results.

B.2 Create Common SGs

ANSYS-SwiftComp GUI provides a convenient way to create some common SG models. Engineers can easily create the geometry and mesh of these models, and invoke SwiftComp^{TM} to perform homogenization and dehomogenization for different composites with arbitrary fundamental building blocks (aka SGs).

Currently, ANSYS-SwiftComp GUI provides the following common SGs:

1D SGs: *layered materials, laminates.*

2D SGs: *square pack microstructures (with interphase region), hexagonal pack microstructures (with interphase region).*

3D SGs: *square pack microstructures, spherical inclusion microstructures.*

This appendix mainly focuses on introducing 1D and 2D common SGs for plates/shells model as this thesis only uses 1D and 2D SGs. For 3D or even customized SGs, please refer to ANSYS-SwiftComp GUI manual, which can be downloaded from cdmHUB [19].

There are three different ways to generate 1D SGs for laminates. The fastest way to generate 1D SG for laminate is to use Fast Generate function: Preprocessor → Common SG → 1D SGs → Fast Generate. Users can use simple notation to define ply sequence from the bottom to the top. For example, case 2 uses the notation [0/90/45/-45/30/-30/75/-75] to indicate ply sequence. Choose the material number for each lamina and assign thickness for each ply as shown in Figure B.2. Both case 1 and case 2 use Fast Generate function. Note: for Solid Model, 2-noded elements will be sufficient. And for Plate/Shell Model, 5-noded elements are needed.

After inputting all the parameters, click OK. The 1D SG for the laminate of case 2 has been created as shown in Figure B.3. Note that Fast Generate function only deals with constant layer thickness and single material property. As shown in Figure B.3, each layer with five nodes has been shown by five different color lines.

If users want to create laminates with different layer thickness and material property, Advanced Generate function in 1D SGs can serve this purpose. Preprocessor →

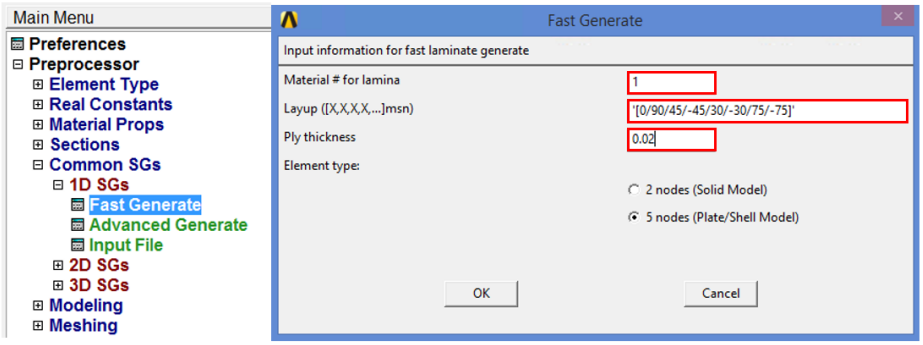

Figure B.2. Fast Generate function

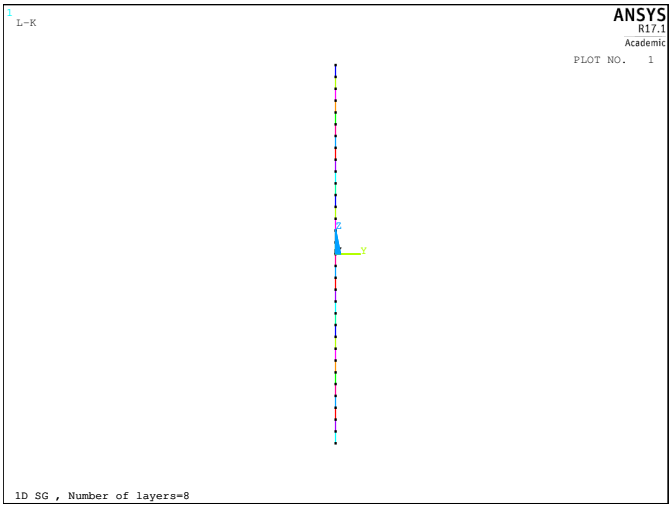

Figure B.3. 1D SG for case 2

Common SG → 1D SGs → Advanced Generate. Choose a laminate [0/90/45/-45] with thickness 0.01 as an example, the input parameters for this laminate is shown in Figure B.4.

In addition, the function of 1D SGs also provides Input File function to let users upload their own data file. This function can handle laminates with complex ply sequence. Click Input File function in the 1D SGs menu. Preprocessor → Common SG → 1D SGs → Input File. A new window will pop out. Users can choose the

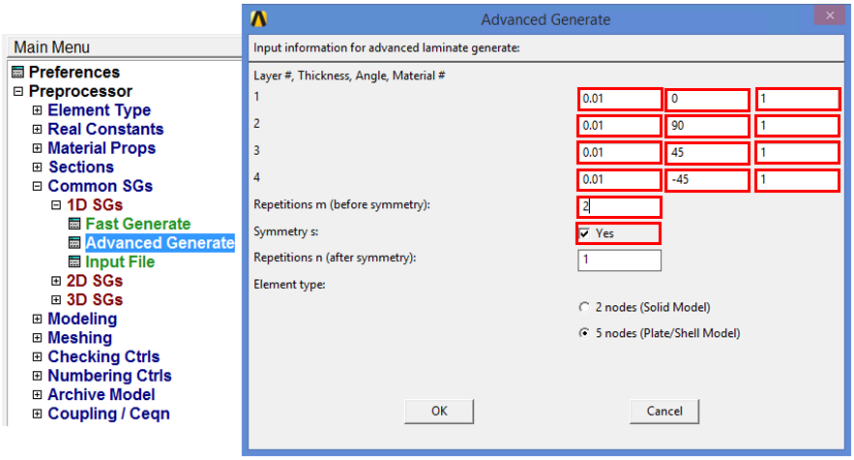

Figure B.4. 1D SG for case 2

file which contains laminate data. The format of the data file is discussed in the ANSYS-SwiftComp GUI Manual. The case 3 uses Input File function to generate the corresponding 1D SG.

The fastest ways to generate common 2D SGs is to use 2D SGs menu: Preprocessor → Common SGs → 2D SGs. For example, if we want to create a square pack microstructure. Choose Square Pack function in 2D SGs menu. Input volume fraction of fiber and keep volume fraction of interphase empty or zero if there is no interphase region in your model. Select corresponding material number for the fiber and matrix. If there is no interphase, keep the Material # for Interphase empty or zero. Select element type and mesh size as shown in Figure B.5. Click OK, The 2D SG represented as a square with a circle in the center will be shown in Figure B.6.

B.3 Homogenization and Dehomogenization

After creating SGs, users can perform homogenization and dehomogenization in ANSYS-SwiftComp GUI, which is explained in the following

Homogenization

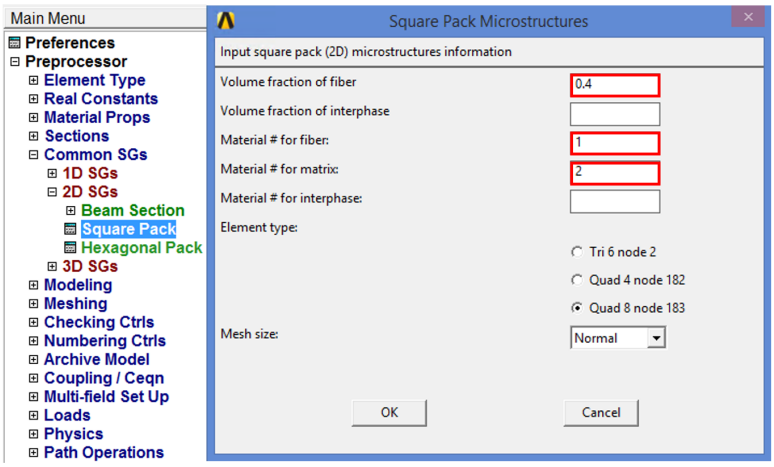

Figure B.5. Square Pack function for common 2D SG

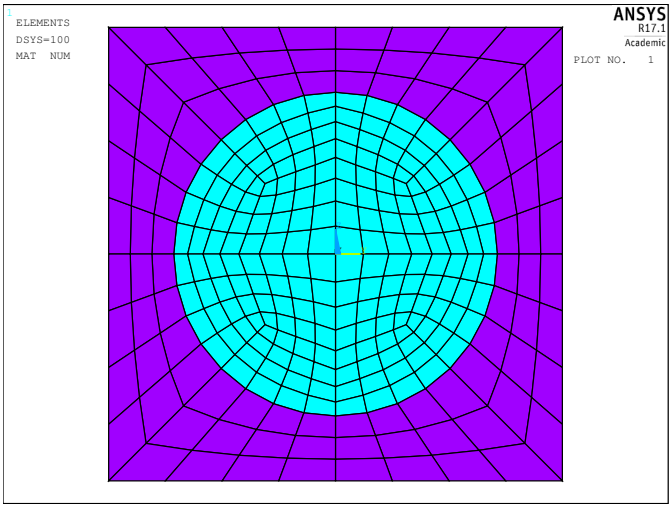

Figure B.6. 2D SG for square pack microstructure

For laminates, the mesh has been generated right after defining 1D SG. Users can directly go to Homogenization function to get the effective properties of a laminate. Preprocessor → Solution → Homogenization → Plate/Shell Model. We will use the model generated by case 5 to show the results of Homogenization and Dehomogenization. Click Plate/Shell Model in Homogenization function, keep default parameters

and Click OK as depicted in Figure B.7. Then the effective properties will pop up automatically as shown in Figure B.8.

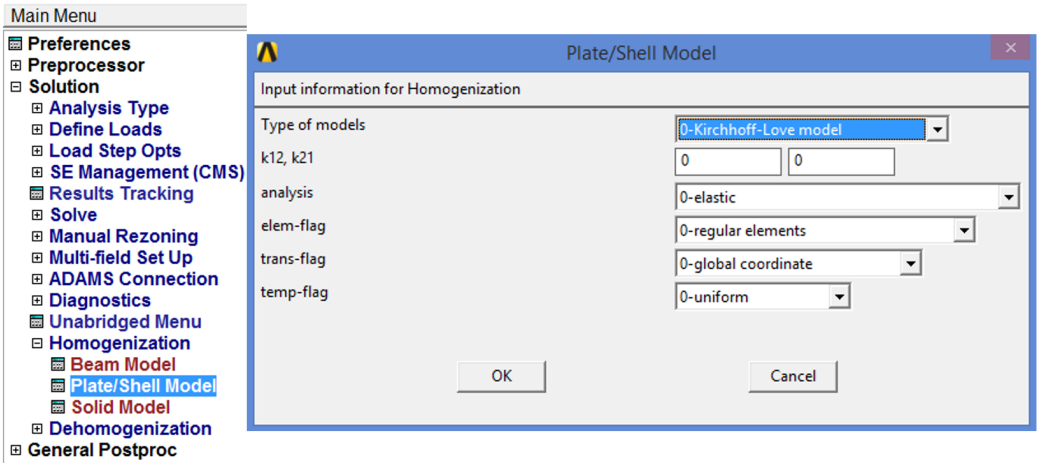

Figure B.7. Plate/Shell Model function for Homogenization

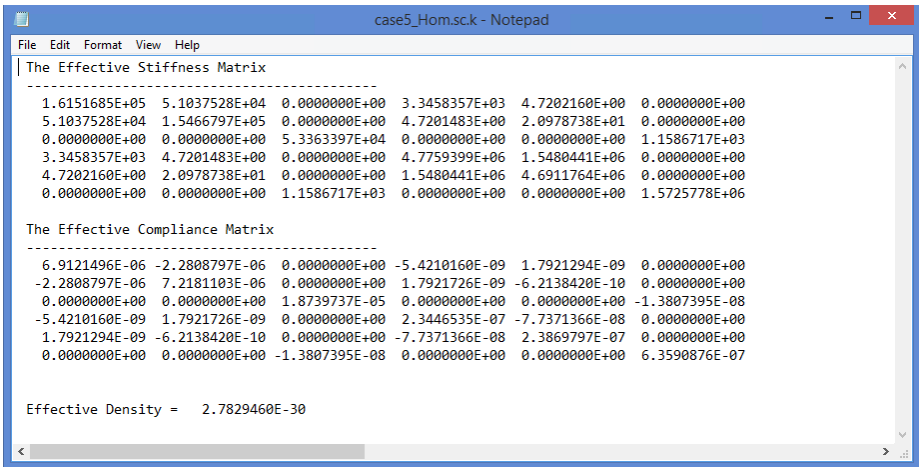

Figure B.8. Effective properties for case 5

Dehomogenization

Before dehomogenization, users need to perform structural analysis in ANSYS to get global behavior. This step can be done independently by using ANSYS. The only additional step needed is to read A, B, D and G matrices from homogenization analysis, which can be easily done by using *sectype,1,gens* command. Then go to Pre-

processor → Solution → Dehomogenization → Plate/Shell Model. Input the global behavior from the plate analysis as depicted in Figure B.9. Click Run. The post-processing results will be automatically loaded. The default value is the magnitude of displacement as in Figure B.10.

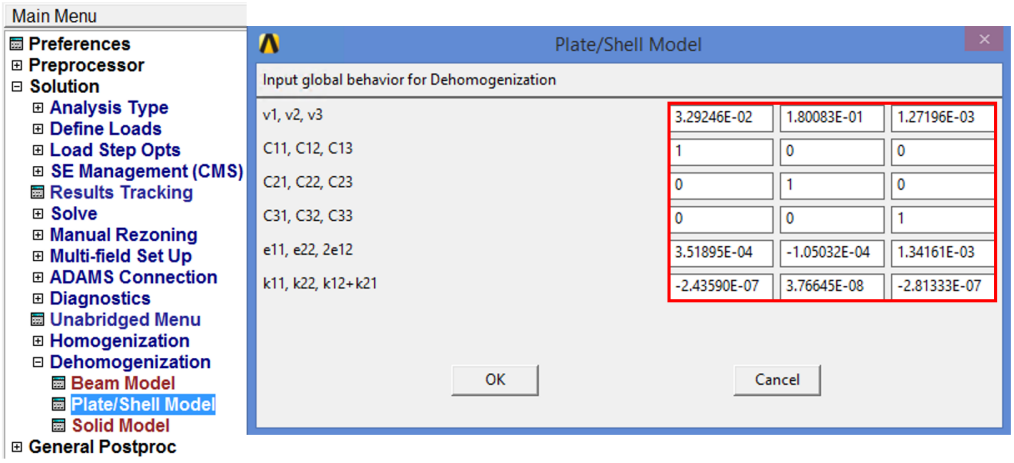

Figure B.9. Plate/Shell Model function for Dehomogenization

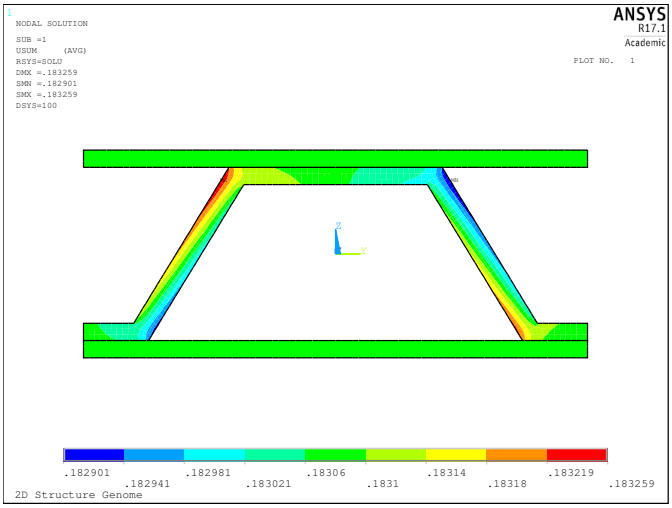

Figure B.10. The magnitude of displacement for case 5